

## ABSTRACT

Title of Document: IN SITU PROCESSING OF PtSn  
ELECTROCATALYSTS FOR CO  
TOLERANCE IN PEM FUEL CELLS

Robert Utz, Master of Science, 2011

Directed By: Professor Greg Jackson  
Department of Mechanical Engineering

Improved anode CO tolerance is a promising approach for integrating low-temperature PEM fuel cells with hydrocarbon fuel processors in cost-effective systems for portable and stationary power applications. PtSn@Pt core-shell nanoparticle electrocatalysts – created by applying cyclic potentials in the presence of CO to PtSn intermetallic nanoparticles in rotating disk electrode (RDE) experiments – have demonstrated the potential for high CO tolerance at low temperatures. This study explores the use of potential cycling with full PEM fuel cell membrane electrode assemblies (MEAs), initially with PtSn anode electrocatalysts, to produce PtSn@Pt electrocatalysts in situ for increased anode CO tolerance. Potential cycling of PtSn anodes in MEAs with various gaseous feeds consistently showed less dramatic decreases in CO oxidation overpotentials than observed in RDE studies. Although some results suggested that modified PtSn electrocatalysts outperform state-of-the-art PtRu anode electrocatalysts, PtSn@Pt electrocatalysts formed via MEA potential cycling consistently

did not provide adequately low anode overpotentials with CO up to 1000 ppm to outperform commercial PtRu anode catalysts. Energy-dispersive X-ray spectroscopy of MEA cross-sections showed that Sn leached from the anode into the cathode as the number of cycles increased. Consistent formation of PtSn@Pt core-shell structures for high CO tolerance in full MEAs remains a challenge for further investigation.

In situ processing of PtSn electrocatalysts for CO tolerance in PEM fuel cells

By

Robert Christopher Utz

Thesis submitted to the Faculty of the Graduate School of the  
University of Maryland, College Park, in partial fulfillment  
of the requirements for the degree of  
Master of Science  
2011

Advisory Committee:  
Professor Gregory Jackson, Chair  
Professor Bryan Eichhorn  
Professor Michael Zachariah

© Copyright by  
Robert Christopher Utz  
2011

## Acknowledgements

The contributors to this thesis are many and I am extremely grateful for their assistance.

My advisor, Dr. Greg Jackson, always encouraged me to extend my knowledge and skills a little further and was able to keep me, as well as all of us in the research group, on the right path even when progress was difficult and setbacks threatened to discourage. Both Zhufang Liu and Chris Sims provided all of the catalyst fabrication and RDE characterization and helped me understand facets of their work that enriched my understanding of catalysis. Their work, along with the helpful guidance of Dr. Bryan Eichhorn, provided an alternative perspective that proved valuable in my research. Larry Lai in the NISPLab helped me perform SEM images and EDX analysis, which would have been difficult to complete without his assistance. Ian Young taught me many experimental techniques and equipment fixes that now seem natural to me. This work was sponsored by the Army Research Office as part of a project involving Ballard Power Systems and their team on-site at the University of Maryland. Pat Hearn, Chris Tesluk, Greg Hoeschele, and others answered questions that I had and labored side by side me on their own PEM fuel cell project to which my work could become relevant if successfully taken to the limits.

Will Gibbons, Atul Bhargav, Rick Stroman, Josh Pearlman, Chris Maxey, Anita Maghdouri, Jennie Moton, and all the members of the Jackson research group who shared the graduate student life with me and supported me through it all. My roommate Tim Natriello traversed his own graduate school journey and was a good friend along the way. My parents and sister Holly gave me encouragement when I needed it the most and were

always just a drive away. They have given me unlimited support and unconditional love that I could always fall back upon. My friends back in Baltimore and Boston helped me take much-needed breaks and relax when I was most stressed. Finally, Sarah Stricker has made me happier than I have ever been, even during the most difficult times in my graduate career.

## Table of Contents

Acknowledgements .....	ii
Table of Contents .....	iv
List of Figures .....	v
List of Tables .....	viii
List of Abbreviations .....	ix
1 Introduction .....	1
1.1 PEM Fuel Cell Systems and CO-Tolerant Anodes .....	1
1.2 Principles of PEM Fuel Cells .....	3
1.3 Anode Electrocatalyst Development for CO Tolerance .....	8
1.4 Objectives and Outline of Thesis .....	13
2 Experimental Methods .....	16
2.1 MEA Fabrication .....	16
2.1.1 Catalyst Formation and Characterization .....	18
2.1.2 Ink Preparation .....	19
2.1.3 Catalyst Application .....	20
2.1.4 MEA Pressing .....	20
2.2 In Situ MEA Catalyst Processing .....	21
2.2.1 MEA Test Fixture and Instrumentation .....	21
2.2.2 Potential Cycling .....	23
2.3 MEA Characterization .....	32
2.3.1 Electrochemical Characterization .....	32
2.3.2 Ex situ Catalyst Characterization .....	33
3 Electrochemical Results of Potential Cycled Anodes .....	36
3.1 Potential Cycling for In Situ Electrocatalyst Modification .....	36
3.1.1 Variation of Cycles between Characterization .....	37
3.1.2 Variation of Potential Cycling Range .....	45
3.1.3 Variation of Gas Composition .....	48
3.2 Electrochemical Performance on CO-Laden Fuels .....	56
3.2.1 Polarization Curves .....	56
3.2.2 EIS .....	63
3.3 Conclusion .....	72
4 Ex situ Catalyst Characterization .....	74
4.1 SEM/EDX of Catalyst Layer .....	74
4.2 Conclusion .....	81
5 Conclusions .....	82
5.1 Significant Results and Impact on PEM Fuel Cell Systems .....	82
5.2 Recommendations for Future Work .....	84
Bibliography .....	87

## List of Figures

<b>Figure 1.1:</b> H <sub>2</sub> adsorption, O <sub>2</sub> adsorption, and charge transfer reaction pathways in a PEM fuel cell MEA with current .....	6
<b>Figure 1.2:</b> Voltage-current plots in a PEM fuel cell MEA with H <sub>2</sub> /CO anode fuel and showing CO overpotential using 30% wt Pt/C catalyst at 80°C cell temperature, 0.22 MPa H <sub>2</sub> , 0.24 MPa O <sub>2</sub> (adopted from Oetjen [21]).....	7
<b>Figure 1.3:</b> Polarization data for MEA using 20% wt PtRu (1:1.5) anode catalyst for up to 1000 ppm CO. 2.2/2.2 stoichiometry with 0.56/0.133 SLPM minimum flow rates, 70 °C cell temperature with 70 °C anode and cathode dew points.....	13
<b>Figure 2.1:</b> The single MEA test fixture showing the flow paths in the current collection plates and the MEA mounted onto one half of the test fixture.....	22
<b>Figure 2.2:</b> Distribution of potential relative to RHE across a PEMFC MEA showing how $V_{cell}$ decreases from $V_{OCV}$ as current is applied and again as CO is added to the anode .....	26
<b>Figure 2.3:</b> SEM image of MEA 4b after testing, 300X magnification.....	35
<b>Figure 3.1:</b> Polarization for CO oxidation using 1000 ppm CO using various anode electrocatalysts in RDE experiments: 298 K, 1mV/s scan rate, 1600 RPM, 0.5 M H <sub>2</sub> SO <sub>4</sub> electrolyte solution (taken from Liu et al. [32]).....	38
<b>Figure 3.2:</b> Current during potential cycle 1, 50, 100, and 200 of MEA 8b as a function of (a) cell voltage and (b) calculated anode potential. Cycles performed at 70 °C, OCV to -0.2 V cell potential range, 0.1/0.15 SLPM anode/cathode flow rates.....	39
<b>Figure 3.3:</b> Effect of cycles between characterization, MEA 8b: (a) 400 cycles and (b) 200 cycles. Cycles performed at 70°C, OCV to -0.2 V potential range, 0.1/0.15 SLPM anode/cathode flow rates .....	42
<b>Figure 3.4:</b> Comparison of cycle set size in post-cycling polarization of MEA 7a at 0 ppm (a) and 25 ppm (b) 2.2/2.2 stoichiometry with 0.56/0.133 SLPM minimum flow rates, 70 °C cell temperature with 70 °C anode and cathode dew points.....	43
<b>Figure 3.5:</b> Comparison of cycle set size in post-cycling polarization of MEA 7b at 0 ppm (a) and 25 ppm (b): 2.2/2.2 stoichiometry with 0.56/0.133 SLPM minimum flow rates, 70 °C cell temperature with 70 °C anode and cathode dew points.....	44
<b>Figure 3.6:</b> Comparison of cycle set size in post-cycling polarization of MEA 8a at 0 ppm (a) and 25 ppm (b): 2.2/2.2 stoichiometry with 0.56/0.133 SLPM minimum flow rates, 70 °C cell temperature with 70 °C anode and cathode dew points.....	46

<b>Figure 3.7:</b> Comparison of cycle set size in post-cycling polarization of MEA 8a at 0 ppm (a) and 25 ppm (b): 2.2/2.2 stoichiometry with 0.56/0.133 SLPM minimum flow rates, 70 °C cell temperature with 70 °C anode and cathode dew points.....	47
<b>Figure 3.8:</b> CO cycling procedure, first, 200 <sup>th</sup> , and last cycle at end of cycling, MEA 9c. Cycles performed at 70°C, OCV to 0 V cell potential range, 0.34/0.15 SLPM anode/cathode flow rates .....	50
<b>Figure 3.9:</b> CO cycling procedure for MEA 9c, 400 <sup>th</sup> and last cycle of each set for sets 1 through 4 and set 8. Cycles performed at 70°C, OCV to 0 V cell potential range, 0.34/0.15 SLPM anode/cathode flow rates.....	51
<b>Figure 3.10:</b> CO cycling procedure, MEA 4b (a) cycles 400 to 600 (b) cycles 600 to 800 with H <sub>2</sub> cathode gas and 1000 ppm CO anode gas. Cycles performed at 70°C, OCV to 0.4 V cell potential range, 0.1/0.1 SLPM anode/cathode flow rates .....	53
<b>Figure 3.11:</b> CO cycling procedure, MEA 4b (a) cycles 800 to 1000 (b) 100 <sup>th</sup> cycle of each set with H <sub>2</sub> cathode gas and 1000 ppm CO anode gas. Cycles performed at 70°C, OCV to 0.4 V cell potential range, 0.1/0.1 SLPM anode/cathode flow rates.....	54
<b>Figure 3.12:</b> Balance gas comparison: 200 potential cycles with H <sub>2</sub> balance gas followed by 200 potential cycles with N <sub>2</sub> balance gas. Cycles performed at 70°C, OCV to 0.4 V cell potential range, 0.1/0.1 SLPM anode/cathode flow rates .....	56
<b>Figure 3.13:</b> Polarization data of MEA (a) 4b and (b) 7a, potential cycled PtSn anode catalyst with up to 1000 PPM CO. 2.2/2.2 stoichiometry with 0.56/0.133 SLPM minimum flow rates, 70 °C cell temperature with 70 °C anode and cathode dew points.	59
<b>Figure 3.14:</b> Polarization data by MEA (a) 7b and (b) 8a potential cycled PtSn anode catalyst with up to 1000 PPM CO. 2.2/2.2 stoichiometry with 0.56/0.133 SLPM minimum flow rates, 70 °C cell temperature with 70 °C anode and cathode dew points.	60
<b>Figure 3.15:</b> Polarization data of MEA (a) 8b and (b) 9c, potential cycled PtSn anode catalyst with up to 100 PPM CO. 2.2/2.2 stoichiometry with 0.56/0.133 SLPM minimum flow rates, 70 °C cell temperature with 70 °C anode and cathode dew points.....	61
<b>Figure 3.16:</b> PtSn(3:1) anode electrocatalyst polarization curve from Lee, Hwang, Lee (2005) at 0 ppm, 10 ppm, 50 ppm, and 100 ppm CO at 80 °C .....	62
<b>Figure 3.17:</b> EIS Nyquist plot of MEAs 7a, 7b, and 9c at a) 100 mA/cm <sup>2</sup> and b) 500 mA/cm <sup>2</sup> under polarization data operating conditions .....	65
<b>Figure 3.18:</b> EIS Nyquist plot of MEAs (a) 8a, (b) 8b, and (c) PtRu at 100 and 500 mA/cm <sup>2</sup> under polarization data operating conditions .....	66

<b>Figure 3.19:</b> MEA 8a performance transformation after 4 <sup>th</sup> , 5 <sup>th</sup> , and 6 <sup>th</sup> cycling sets at 0, 25, 50 and 100 ppm: a) Polarization and b) EIS Nyquist plots at 100 mA/cm <sup>2</sup> under polarization data operating conditions .....	70
<b>Figure 3.20:</b> Shift in onset of $\eta_{CO}$ – (a) Polarization curve of MEA 8a with 25 PPM CO and (b) Current as a function of anode flow channel distance.....	71
<b>Figure 4.1:</b> SEM image of MEA 8a at 300X magnification, catalyst layer separation and dispersed GDL/catalyst segments .....	74
<b>Figure 4.2:</b> SEM image of MEA 7b at 300X magnification, no membrane visible .....	75
<b>Figure 4.3:</b> SEM image of an MEA after fabrication showing intact catalyst layers attached to the membrane at 300X magnification.....	76
<b>Figure 4.4:</b> EDX analysis of PtSn MEA before testing, Pt and Sn content by location...	77
<b>Figure 4.5:</b> EDX analysis of MEA 4b after testing, Pt and Sn content by location.....	78
<b>Figure 4.6:</b> EDX analysis of MEA 8a after testing, Pt and Sn content by location.....	79
<b>Figure 4.7:</b> EDX analysis of MEA 9c after testing, Pt and Sn content by location.....	80

## List of Tables

<b>Table 2.1:</b> CO potential cycling operating conditions.....	27
<b>Table 2.2:</b> Anode gas composition by MEA, by percentage .....	29
<b>Table 2.3:</b> Stoichiometric ratio by MEA, calculated at 1 A .....	30
<b>Table 2.4:</b> Final OCV during CO cycling and cycling limit in V, by MEA.....	31
<b>Table 3.1:</b> Bulk resistance ( $R_{bulk}$ ) of MEAs, calculated from EIS ( $\Omega$ ).....	63
<b>Table 3.2:</b> Polarization resistances at 100 and 500 mA/cm <sup>2</sup> , calculated from EIS ( $\Omega$ ) ...	67

## List of Abbreviations

### Symbols

$i$	current density
$\eta_a$	anode overpotential
$\eta_c$	cathode overpotential
$\eta_{CO}$	CO overpotential
$R_{pol,CO}$	polarization resistance from CO
$V_{cell}$	cell voltage
$V_{OCV}$	open circuit voltage

### Acronyms

ASR	area specific resistance
CV	cyclic voltammetry
DFT	density functional theory
EDX	energy-dispersive X-ray spectroscopy (also EDS)
EIS	electrochemical impedance spectroscopy
FC	fuel cell
FRT	fiberglass-reinforced Teflon
GDE	gas diffusion electrode
GDL	gas diffusion layer
HOR	hydrogen oxidation reaction
HT	high temperature
IPA	isopropyl alcohol / isopropanol
LSV	linear sweep voltammetry

LT low temperature

MEA membrane electrode assembly

OCV open circuit voltage

ORR oxygen reduction reaction

PEM proton exchange membrane or polymer electrolyte membrane

PFA perfluoroalkoxy – fluoropolymer used as gasket material

PSA pressure swing adsorption

PrOx preferential oxidation (of CO)

RDE rotating disk electrode

SCE standard calomel electrode

SEM scanning electron microscope

TEM transmission electron microscope

XPS X-ray photoelectron spectroscopy

XRD X-ray diffraction

# 1 Introduction

## 1.1 PEM Fuel Cell Systems and CO-Tolerant Anodes

Despite the growth of the fuel cell industry and the potential of proton-exchange membrane fuel cells (PEMFCs) for implementation in different power applications, many PEMFC markets in portable and stationary power have not been realized because of the need to develop cost-effective systems that run on available hydrocarbon fuels. Low-temperature ( $< 100\text{ }^{\circ}\text{C}$ ) PEMFCs (LT-PEMFCs) operate using the hydrogen oxidation reaction, with pure  $\text{H}_2$  as the ideal fuel.  $\text{H}_2$  must be extracted from other compounds, such as by splitting  $\text{H}_2\text{O}$  or by reforming hydrocarbons, before it can be used as the anode fuel in a PEM fuel cell. Reforming hydrocarbons such as methane [4] or diesel fuel [3] is currently the most common mode for producing  $\text{H}_2$  because hydrocarbons are readily available with high energy density suitable for transportation and portable power applications. Reforming hydrocarbons, through endothermic steam reforming and/or exothermic partial oxidation, produces a  $\text{H}_2$ -rich reformat stream that contains not only  $\text{H}_2$ , but also  $\text{CO}_2$ ,  $\text{CO}$  and additional  $\text{H}_2\text{O}$  [3, 4, 5]. The presence of  $\text{CO}$  in reformat (to concentrations even below 100 ppm) inhibits  $\text{H}_2$  oxidation on typical LT-PEMFC anode electrocatalyst (generally Pt-based) because  $\text{CO}$  adsorbs strongly to Pt at these temperatures without significant oxidation. This  $\text{CO}$  poisoning tends to be reversible but requires interruption in fuel cell operation either through extreme voltage cycling or exposure of the anode to substantial air, both of which interrupt or compromise the PEMFC power production [6].

Because of the  $\text{CO}$ -poisoning of LT-PEMFC anodes, many technologies have been developed to clean the reformat of  $\text{CO}$  upstream of the fuel cell such that LT-

PEMFCs can be integrated with hydrocarbon reformers. Technologies include Palladium- (Pd-) based membranes, preferential CO oxidation (PrOx) reactors, and pressure-swing absorption (PSA) systems. Pd-based membranes selectively diffuse hydrogen due to a partial pressure ( $P_{H_2}$ ) gradient across the membrane, but they require near-pinhole free processing and the  $P_{H_2}$  gradient requires pressurized reformers for adequate  $H_2$  fluxes for cost-effective designs. Even with high driving  $P_{H_2}$ , Pd-based membrane designs can require large quantities of Pd metal, which can make the cost of a PEMFC fuel cell system prohibitively high. Pressure swing adsorption (PSA) reactors are another reformate purification option that uses adsorption beds with strong affinities for CO [7]. PSA systems can generate reformate streams with almost complete CO removal, but utilize large reactors and require regenerative processes to regain original effectiveness. An alternative method involves injecting a small amount of air into the reformate stream and running it over a selective catalyst (typically based on precious metals) in a PrOx reactor. To keep PrOx reactors highly selective to CO, they must be kept in a narrow-temperature range typically below 200 °C [8, 9, 10] and thus they can require significant cooling. PrOx can be completed in the anode with intermittent air injection to oxidize CO adsorbed on the catalyst surface, but this comes at a penalty of reduced fuel cell performance and durability [11, 12].

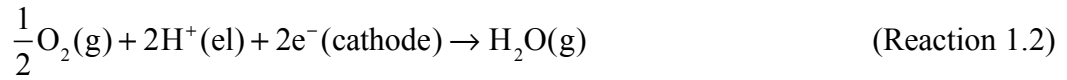
More recent developments in high temperature PEMFCs (HT-PEMFCs) using new polymer membranes typically with phosphoric-acid ( $H_3PO_4$ ) doping have been developed to operate at temperatures between 140 and 180 °C [13, 14, 15, 16]. At these temperatures, PEMFC anode catalysts show excellent CO tolerance at up to 2% CO in the anode stream. However, the HT-PEMFC electrolyte membranes do not provide the

same conductivity (and thus high current densities) as LT-PEMFC Nafion membranes, and the attack of the mobile  $\text{H}_3\text{PO}_4$  causes the HT-PEMFC catalyst to lose activity and limits durability of HT-PEMFCs. The lower power densities and higher catalyst loadings of HT-PEMFCs combined with their relatively poor durability limit their suitability for many fuel cell applications with hydrocarbon fuels to date [15, 16]. Advances in HT-PEMFC membranes and catalyst layers may cause this technology to become more commercially viable in the future.

An alternative approach to handling reformat CO that has spurred significant research involves development of LT-PEMFC anode catalysts that can provide CO oxidation at low-temperatures. Catalyst designs which could provide high power density without significant losses in current and power density, would allow for the durable and more cost-effective LT-PEMFCs to be more simply integrated with hydrocarbon reformers for cost-effective fuel cell systems. This thesis presents an attempt to develop a fabrication process to produce such CO-tolerant catalysts based on recent advances in nano-architected Pt-alloy catalysts for LT-PEMFC anodes [33, 34, 35].

## **1.2 Principles of PEM Fuel Cells**

PEM fuel cells are currently the most widely used type of fuel cell for both portable and stationary applications. The PEMFC uses  $\text{H}_2$  as the fuel source and oxygen as the oxidant through the hydrogen oxidation reaction (HOR) and  $\text{O}_2$  reduction reaction (ORR), described in the global half-cell reactions given here:



The differences in effective  $\text{H}_2$  partial pressure on the anode and cathode side create a voltage,  $V_{\text{cell}} (= \phi_{\text{cathode}} - \phi_{\text{anode}})$  across the membrane-electrode assembly (MEA) and drives the flow of protons through the electrolyte and electrons through electronic conductors from the anode to the cathode to produce electric power. Catalysts (typically Pt-based) are used on both sides of the electrolyte membrane to dissociatively adsorb the reactant gases in a so-called catalyst layer adjacent to the membrane. The anode and cathode absorption reactions on a Pt catalyst are shown here: in



An LTPEMFC MEA usually consists of a thin Nafion proton exchange membrane sandwiched between two gas diffusion electrodes (GDE). The GDE consists of a porous, electrically conductive medium known as a gas diffusion layer (GDL) with an active catalyst layer applied at the interface between the GDL and the membrane. The catalysts for Reactions 1.1 – 1.4 in the catalyst layer must be in contact with the electrolyte to conduct protons to/from the membrane.

The PEMFC MEA is sandwiched between two gas flow channels, typically made of graphite to ensure good electrical conductivity between the GDE and the flow channels. In LT-PEMFCs, the Nafion electrolyte membrane transports  $H^+$  ions across to the cathode when sufficiently hydrated but is not electrically conductive. If not properly hydrated, the Nafion membranes cannot transport the protons and the performance of the fuel cell suffers. For this reason, LT-PEMFCs with typical Nafion electrolyte membranes are limited to operating temperatures less than  $100^{\circ}C$ , above which water will evaporate and deprive the membrane of its proton conductivity. The cathode half reaction (Reaction 1.2) completes the electrochemical process by reducing dissociated oxygen present and forming water with protons supplied through the membrane and electrons supplied from the electrode. Flow channel plates (bipolar plates) also serve as current collectors and the two endplates in a stack of cells are connected to an external power circuit. Multiple MEAs in a fuel cell stack provide large voltages for power applications, but basic fuel cell characterization is often done with single MEA tests as in this study. A diagram of the segments of a PEM fuel cell MEA and their roles in producing an external current is shown in **Figure 1.1**. Further details not directly relevant to this study can be found in PEMFC technology reviews [1, 2].

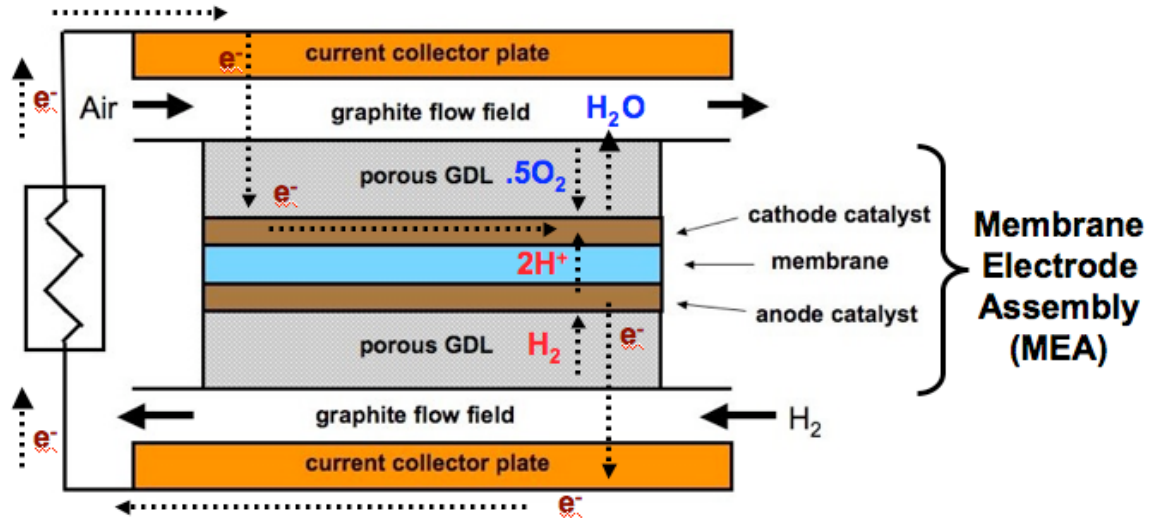
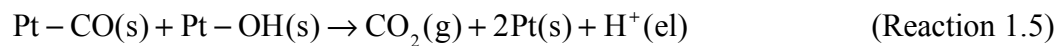


**Figure 1.1:**  $H_2$  adsorption,  $O_2$  adsorption, and charge transfer reaction pathways in a PEM fuel cell MEA with current

Although better for proton conductivity with Nafion, operating temperatures below  $100^\circ C$  result in slow CO oxidation on Pt with a high activation energy barrier.



If CO is present in the anode flow, poor CO oxidation leads to high CO coverages on the Pt sites, which blocks  $H_2$  adsorption. Rotating disk electrode (RDE) experiments using a pure Pt catalyst have shown a high CO fractional surface site coverage of 0.81 at room temperature when CO is bubbled through  $HClO_4$  for 10 minutes [17] and confirmed that CO covered Pt surfaces prevent the  $H_2$  oxidation reaction from taking place [18]. This results in significantly lower currents at desired operating  $V_{cell}$  (typically  $> 0.6 V$ ) compared to a non-CO covered electrode [17, 18]. To remove the CO from the anode, the anode potential must be raised (relative to a reversible  $H_2$  electrode at 0.0 V) to much

closer to the cathode voltage in order to oxidize the CO off of the Pt. This greatly reduces  $V_{\text{cell}} (= \phi_{\text{cathode}} - \phi_{\text{anode}})$ . For a given current density, the reduction in voltage due to the presence of CO is often referred to as a CO overpotential ( $\eta_{\text{CO}}$ ). CO overpotentials implies significantly decreased power density when compared to currents using pure H<sub>2</sub> anode fuel streams [19, 20, 21]. An example of this effect in a PEM fuel cell with Pt anode catalyst from Oetjen [21] is shown in **Figure 1.2**.

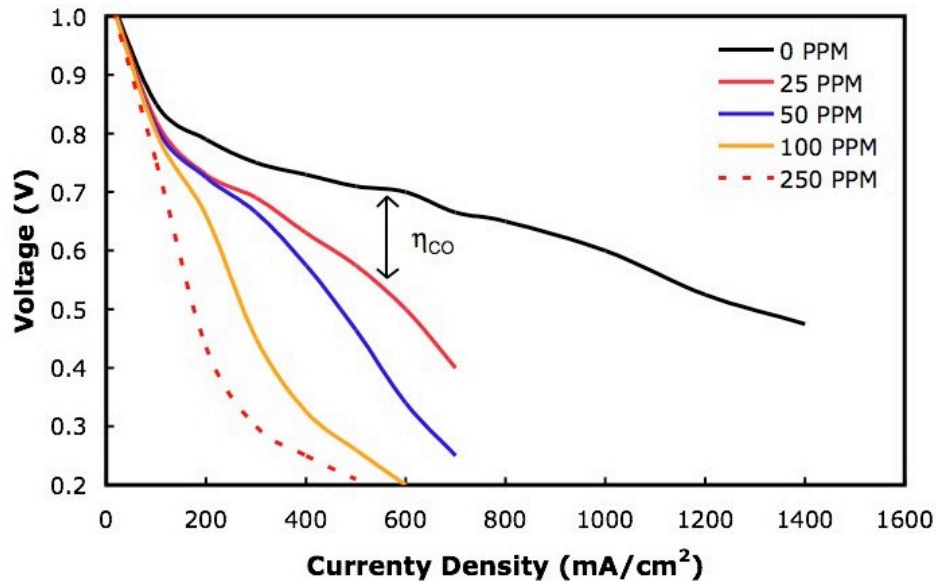


**Figure 1.2:** Voltage-current plots in a PEM fuel cell MEA with H<sub>2</sub>/CO anode fuel and showing CO overpotential using 30% wt Pt/C catalyst at 80°C cell temperature, 0.22 MPa H<sub>2</sub>, 0.24 MPa O<sub>2</sub> (adopted from Oetjen [21])

CO overpotentials in PEM fuel cell anodes are generally reversible, such that over the short term, performance can return to normal over time after restoring pure H<sub>2</sub> fuel. CO exposure can have some long-term detrimental effects on PEM fuel cells. When

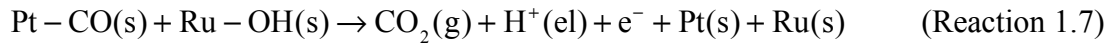
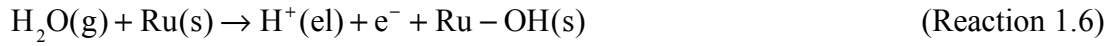
alternating between open circuit and constant current operation, cell voltage has been shown to decay faster with small amounts of CO present than with pure H<sub>2</sub> only [22].

### **1.3 Anode Electrocatalyst Development for CO Tolerance**

Efforts to develop CO-tolerant anode electrocatalysts for LT-PEMFCs have largely focused on platinum alloys. Pt-alloys are heavily researched for two reasons. A Pt-alloy nanoparticle can have very different adsorption properties than pure Pt, which may allow for better CO tolerance when used as an anode electrocatalyst. Pt costs also encourage the use of alloys. Alloying Pt with a cheaper metal would decrease the overall cost of the catalysts, which is not an insignificant portion of the cost of manufacturing an entire PEM fuel cell system.

Several different Pt alloys have been explored for their CO tolerance in PEMFC anodes. Gustavo et. al. showed that PtRu, PtFe, PtMo, and PtW electrocatalysts have shown excellent CO tolerance at a CO concentration of 100 ppm using common operating parameters [24]. Lee, Mukerjee, et al, have performed multiple studies on PtRu and PtSn for their CO tolerance capabilities with different results for each catalyst [25, 26, 27]. Different ratios of elements in Pt alloys may change the activity of the catalyst as well, as seen in ethanol oxidation on PtSnOx catalysts [28]. By altering the ratio of Pt to alloying element in the catalyst particle, the total Pt content can be lowered, reducing the overall material cost of the catalyst if the alloying element is more common (Sn, Fe, etc). There are two proposed mechanisms by which Pt-alloys may improve PEM fuel cell performance with CO containing fuel streams. The bi-functional mechanism involves reduction of the CO overpotential by adsorption of oxygen-containing species (specifically OH) on an alloy site to oxidize CO [29]. The CO oxidation reaction behaves

as Reaction 1.6 and 1.7 in PEM fuel cell models with CO reactions included in the anode catalyst layer containing PtRu [30]:



OH forms from water dissociates on the catalyst surface as indicated in Reaction 1.6.

This OH then reacts with CO to remove it from the Pt surface as in Reaction 1.7.

Recent studies have proposed the concept that the structure of Pt-alloy nanoparticles can influence their surface activity as much as the composition. This has led to several studies trying to tailor Pt-alloy nanoparticle structure for high CO tolerance in LT-PEMFC anodes [33]. Intermetallic nanoparticle catalysts, catalysts that have an ordered structure of platinum and alloy elements, have shown promise as CO tolerant catalysts, specifically PtSn and PtSb [1, 32].

Another promising approach for improving CO tolerance involves core-shell nanoparticle catalysts, which have one elemental composition on the surface and another composition in the interior (core) of the particle. An altered arrangement of elements can change the adsorption properties in a catalyst nanoparticle. Core-shell nanoparticle based on PtNi have been explored as ORR catalysts for PEM fuel cells [34,35]. Core-shell nanoparticles have been studied for PrOx catalysts in H<sub>2</sub>-rich environments [33]. Core-shell architectures with Pt shells achieve CO tolerance because the underlying core shifts the d-band centers of the Pt surface atoms. Appropriate shifts in the d-band center can

lower the activation barrier to CO oxidation on the Pt surface which will reduce CO poisoning and allow increased rates for H<sub>2</sub> oxidation [24, 27, 31].

Many alloys and core-shell architectures used oxophilic metals such as W [24], Sn [25, 26, 37, 38], or Fe [24] and these catalysts containing readily oxidized metals are vulnerable to oxidation and/or leaching in the acidic environment of the PEMFC anode. Leached atoms can travel through the electrolyte membrane into other areas of the MEA and interfere with proton conduction in the electrolyte or catalyst activity on either electrode particle. [36]. Core-shell nanoparticles may help prevent this behavior if the shell maintains stability with a relatively stable but active element, notably Pt. It remains to be seen whether these core-shell nanoparticle structures will be stable in an anode. It is clear that both composition and structure are important for the properties of a nanoparticle electrocatalyst.

PtSn electrocatalysts have had mixed results in terms of CO tolerance in PEM fuel cell anodes. In rotating disk electrode (RDE) experiments, the CO oxidation potential is much lower for PtSn than for Pt and even other Pt-alloys like PtRu [32, 37]. This suggests that PtSn may be an excellent CO tolerance anode electrocatalyst. Density functional theory (DFT) modeling suggests that CO oxidation off of a PtSn surface occurs two to four times faster than a Pt surface [39]. In single PEMFC MEA experiments using Nafion-based membranes, PtSn catalysts are still subject to significant CO overpotentials [26, 37, 38]. Polarization curves of MEAs using PtSn electrocatalysts in the anode show a large initial drop in voltage when CO is present at any concentration but then match the slope of the pure H<sub>2</sub> polarization curve in the linear region. At CO concentrations of 100 ppm or greater, PtSn demonstrates higher currents than Pt at typical

operating voltages, but lower currents than PtRu [26, 37, 38]. The discrepancy between RDE and full cell MEA experiments suggests that structure may be an important factor for maximizing CO tolerance in PtSn catalysts. In fact, RDE experiments have demonstrated that PtSn@Pt core shell nanoparticles have the lowest CO oxidation potential and would likely be the best CO tolerant catalyst [32]. Achieving the PtSn@Pt core shell nanoparticle structure would likely result in a more CO tolerant anode electrocatalyst.

RDEs are frequently used to study electrocatalysts. Cyclic voltammetry experiments with RDEs can display at which voltages do processes such as adsorption and desorption of species occur. Extensive research is performed on PEM fuel cell cathode electrocatalysts and their ability to perform the oxygen reduction reaction using RDEs. For anode electrocatalysts, it is unclear if the results obtained from RDE testing for CO tolerance translate to similar behavior in a full MEA. Previous studies using RDEs have shown electrocatalysts such as PtMo alloy and Mo@Pt core-shell with properties indicative of CO activity but did not translate into CO tolerance in a full MEA [47]. RDE experiments for CO tolerance of anode electrocatalysts should always be accompanied by parallel experiments with full MEAs to verify CO activity.

Improvement in anode catalysts for CO tolerance in LT-PEMFCs over state of the art PtRu alloy electrocatalysts could allow for reduced CO-clean up expense. PtRu alloy electrocatalysts have severe voltage losses at CO concentrations of 100 ppm or higher, as seen in **Figure 1.3**. Pt-alloy and core-shell nanoparticle electrocatalysts that have shown impressive CO tolerance capability in RDE experiments have not provided the same significant improvement in performance for CO tolerance in full LT-PEMFC MEA

experiments. One possible explanation for this difference in performance may arise from the fabrication processes involved in forming the catalysts. Nano-structured catalysts often require sequential processes with the use of surfactants or stabilizers on the surface to constrain the nanoparticle growth [27, 48]. Surfactants or stabilizers may interfere with the desired behavior of the catalyst nanoparticle in a PEMFC where in the catalyst must be in intimate, direct contact with electrolyte ionomers that conduct the protons into the membrane. These stabilizers can be difficult to remove without heat treatment or acidic oxidation that may alter the nanoparticle structure [48]. For these reasons, opportunities for anode catalyst research include testing new catalyst nanoparticle structures, alternative fabrication methods for core shell nanoparticles that prevent surfactant interference, and electrochemical methods of creating new catalyst structures inside of the anode catalyst layer.

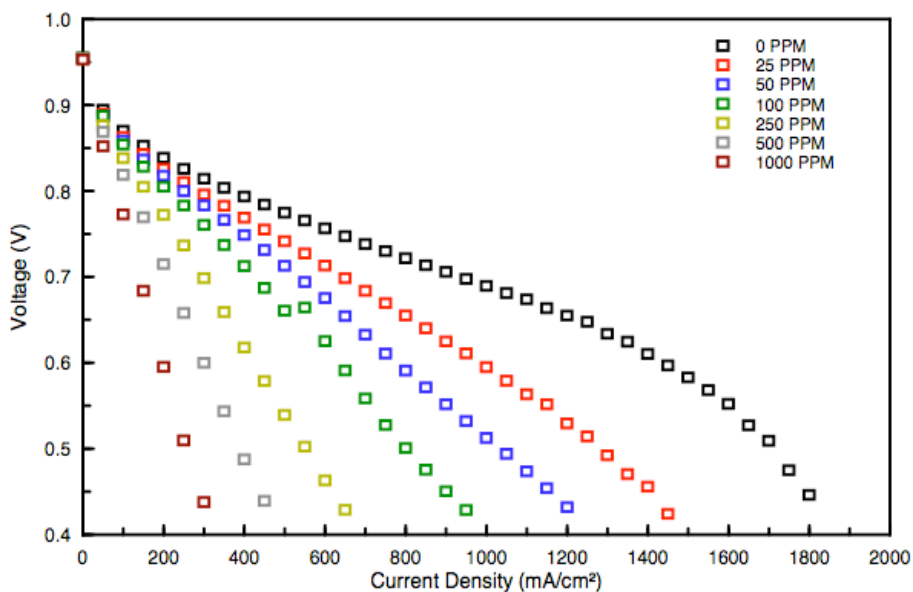


**Figure 1.3:** Polarization data for MEA using 20% wt PtRu (1:1.5) anode catalyst for up to 1000 ppm CO. 2.2/2.2 stoichiometry with 0.56/0.133 SLPM minimum flow rates, 70 °C cell temperature with 70 °C anode and cathode dew points

## 1.4 Objectives and Outline of Thesis

This thesis explores the electrochemical processing of a PtSn intermetallic nanocatalyst to generate a PtSn@Pt core shell structure, which has exhibited effective CO electro-oxidation at low overpotentials in RDE experiments at low-temperature. A similar processing technique to generate a PtSn@Pt structure from PtSn intermetallic on rotating disk electrodes in H<sub>2</sub>SO<sub>4</sub> electrolyte showed significantly improved CO tolerance over Pt, PtSn intermetallic, and industry standard PtRu electrocatalysts. This thesis attempts to recreate that process inside of a full LT-PEMFC MEA and achieve the end result of high CO tolerance due to effective CO oxidation in the anode catalyst layer. Important processing parameters were varied to examine their effect on CO tolerance and catalyst structure stability. MEAs were fabricated in-house using established methods

that were verified using industry supplied PtRu catalyst. The PtRu catalyst was used as a standard for CO tolerance to which the results of this thesis could be compared. There is concern that the catalyst processing procedure can cause Sn to dissolve and migrate across the membrane to the cathode. Post testing characterization was performed to look for scattered Sn particles and look into the nature of the Sn particles themselves in the PtSn@Pt nanoparticles.

The objectives of this study are summarized as follows:

- define processing approach to make core-shell structures in situ to an MEA without unwanted organic stabilizers that disrupt the catalyst/ionomer interface
- explore the effectiveness of PtSn@Pt anode electrocatalysts for CO tolerance in realistic MEA structures with Nafion electrolytes

The subsequent chapters in this thesis lay out the effort to achieve these objectives.

Chapter 2 describes the experimental methods used for fabrication, processing, testing, and post-testing characterization of the MEA. MEA fabrication parameters such as PtSn intermetallic synthesis, ink preparation, and catalyst loading were kept consistent for all MEAs. The testing equipment is listed in detail and the potential cycling procedure described with relevant parameters. The polarization and electrochemical impedance spectroscopy methods are specified and post-testing characterization explained.

Chapter 3 examines the electrochemical results obtained from the testing procedure. Potential cycling experiments were recorded to observe how CO adsorption and oxidation differed between operating conditions and how they proceeded as the number of cycles increased. Polarization data showed the increase in CO overpotential as a function of current from increasing CO concentration. Electrochemical impedance

spectroscopy examines relative impedances of the membrane and catalyst layers and indicates the nature of the chemical processes involved.

Chapter 4 details the characterization results after testing. The MEAs were frozen and cut into cross sectional samples for observation using scanning electron microscopy. The relative amounts of Pt and Sn in both the anode and cathode catalyst layers were detected using energy-dispersive X-ray spectroscopy for both untested and post-cycling MEAs.

Chapter 5 contains conclusions and recommendations for future work. Recommendations for further research include XPS/TEM analysis to examine nanoparticle structure of cycled PtSn, alternative synthesis methods of PtSn@Pt core-shell nanoparticles, and potential cycling methods that utilize fixed reference electrodes.

## 2 Experimental Methods

This chapter will discuss the fabrication and experimental methods used in this study. MEA fabrication techniques are detailed, including catalyst formation, ink preparation, ink application to the gas diffusion layer, and final pressing of the electrodes and membrane. Processing the electrocatalysts with potential cycling under different fuel cell operating conditions to create PtSn@Pt core shell anode catalysts is described and compared with the processes and conditions used in earlier RDE experiments. Electrochemical characterization techniques to explore the anode electrocatalyst activity are detailed. Finally, this chapter will highlight ex situ analysis techniques to assess MEA composition and to investigate possible leaching of Sn during potential cycling and fuel cell operation.

### 2.1 MEA Fabrication

Studies on anode electrocatalysts for PEM fuel cells operating on H<sub>2</sub>-rich reformat focus on how CO concentrations impact voltage-current ( $V-i$ ) relationships and associated anode overpotentials. For LT-PEMFC electrocatalysts, disk electrodes in liquid acidic media are frequently used to study electrochemical performance [39]. These disk electrode experiments use reference electrodes to isolate overpotentials of the specific electrode and thereby to assess the impact of electrocatalyst composition, and structure on activity. This technique has been used extensively for studying O<sub>2</sub> reduction as reviewed nicely elsewhere [41, 42]. Disk electrodes have been used in only a few studies for PEMFC anode electrocatalysis although early studies by Gasteiger et al. [42]

and more recent studies by Liu et al. [32] have shown that disk electrode studies can identify alloy electrocatalysts for CO oxidation.

Rotating disk electrode (RDE) experiments employ linear sweep voltammetry (LSV) and cyclic voltammetry (CV) to minimize transport effects for evaluating electrode overpotentials needed to drive oxidation and/or desorption reactions. For anode electrocatalysts, it remains unclear if the results obtained from RDE testing for CO tolerance translate to similar behavior in a full MEA. Previous studies using RDEs have shown electrocatalysts such as PtMo, with properties indicative of CO activity but did not translate into CO tolerance in a full MEA [47]. The CO oxidation reaction in Reaction 1.6 and 1.7 at the catalyst/ionomer interface in PEMFCs may be influenced by the presence of the liquid phase electrolyte solution. Thus, RDE experiments for CO tolerance of anode electrocatalysts are best accompanied by parallel experiments with full MEAs with gaseous reactant feeds, as done in this study, to verify CO oxidation activity under working fuel cell conditions.

Single PEM fuel cell MEAs of a smaller size are tested to explore new catalyst layers since they provide relatively uniform operating conditions that allow for more straightforward analysis of electrochemical results. Smaller MEAs also conserve material (particularly total weight of catalyst). MEAs with new catalysts developed in this study for CO tolerance are compared to data from commercially available Pt-alloy electrocatalysts operating in both pure H<sub>2</sub> and CO containing anode fuel flows in normal operation. A previous study established an MEA fabrication method used in this study [47] for integrating custom anode catalyst layers with commercial cathodes for LT-

PEMFCs. The method will be briefly summarized here, with modifications for better use with the PtSn catalyst noted where necessary.

### **2.1.1 Catalyst Formation and Characterization**

PtSn intermetallic nanoparticles were produced in-house through methods described previously by Liu et al [32] and reviewed briefly here. PtSn intermetallic nanoparticles were created by reducing Pt(acac)<sub>2</sub> and SnCl<sub>4</sub> in octadecene through the reducing agent NaBEt<sub>3</sub>H. Oleylamine and oleic acid were introduced as surfactants to restrict particle growth and control the final particle size. Vulcan XC-72 powder carbon supports were added to the particles in the weight ratio of 1.83:1 carbon support to Pt(acac)<sub>2</sub> for a 30 weight percent by metal catalyst powder. The powder was added by dispersing the particles and powder in hexane and sonicating. After drying in air, the remaining catalyst was heated at 450°C in Ar/H<sub>2</sub> (5% H<sub>2</sub>) to remove the surfactants.

Transmission electron microscopy (TEM), energy dispersive X-ray spectroscopy, and X-ray diffraction (XRD) were used to characterize the formed particles. TEM images showed an average particle size of 3.5 nm before annealing and the majority of particles between 3 and 5 nm after annealing. EDX showed Gaussian Pt and Sn distributions in the nanoparticles that remained bimetallic and homogenous throughout (1:1 ratio) [32]. XRD patterns from the prepared catalyst showed a hexagonal pattern indicative of PtSn intermetallic particles [32]. PtSn intermetallic catalysts showed improved CO tolerance after cycling in RDE experiments whereas PtSn random alloy particles did not. Distinguishing between the two was a necessary step to take before continuing with MEA fabrication.

### 2.1.2 Ink Preparation

Depositing the catalyst as formed into a PEM fuel cell MEA requires the creation of catalyst ink, which contains the carbon-supported catalyst, the Nafion ionomer solution, and solvents. Dispersing the catalyst into an ink solution allows for ease of application to a gas diffusion layer (GDL) or membrane through painting or spraying. The ink consists of a Nafion-catalyst mixture that allows for better transfer of protons between the membrane and catalyst particles. The catalyst ink was produced as follows. A stock solution was created consisting of 5% Nafion solution (1100 EW) in lower aliphatic alcohols and water, isopropanol, and water. The stock was sonicated for 1 hour in a water bath and transferred to a separate vial containing the carbon-supported catalyst. For every mg of supported catalyst, the stock solution contained 12 mg of 5% Nafion solution, 31 mg of isopropanol, and 20 mg of water. The resulting ink was sonicated for 15-30 minutes with care taken to ensure that overheating of the catalyst did not occur. This process was also used to generate a catalyst ink with PtRu(1:1.5) (TKK) catalyst.

The ideal catalyst ink suspends the catalyst particles in a colloidal suspension while minimizing agglomeration of catalyst particles. Ideally, the catalyst suspension will have a uniform consistency that remains stable throughout the catalyst application process. A successful catalyst ink formula and preparation method ensures the creation of a uniform catalyst layer and allows for consistency between separate MEAs. Multiple catalyst ink preparation methods, including ball milling, probe sonication, alternate stock formulas, and more viscous inks for screen printing on the membrane were attempted without consistent success by previous work [47]. For PtSn anode electrocatalysts, the addition of water to the stock solution helped dissolve catalyst particles better than stock

solutions without water. Since only one catalyst composition was used, one catalyst ink formula and procedure covers all experiments and removes the possibility of inconsistency between different tests.

### **2.1.3 Catalyst Application**

The anode catalyst layers were painted onto the hydrophobic microporous layer of a woven carbon cloth gas diffusion layer (GDL from BASF part # LT1200W) and cut into a 2.2 cm x 2.2 cm square. A paintbrush (5/16" width) was dipped into the catalyst ink and pressed into the side of the vial to remove excess liquid before each coat was applied. The wet GDL was dried at 60°C between each application. The GDL was rotated 90° between each coat for even distribution of the catalyst. The ink was mixed with a magnetic stir bar continuously and sonicated for 5 minutes just before the application of each coat in order to maintain a consistent suspension. As long as the suspension is consistent, the catalyst layer composition can be assumed to be in the same proportion as the catalyst ink without isopropanol. Care must be taken to ensure that this is the case so that calculated catalyst loadings are correct.

### **2.1.4 MEA Pressing**

Before pressing, a 4 cm x 4cm, 50 µm thick Nafion 212 membrane (Ion Power Inc, New Caste, DE) was initially treated for 1 hour in lightly boiling 3% H<sub>2</sub>O<sub>2</sub>, 2 hours in lightly boiling water, and 1 hour in lightly boiling 0.5 M H<sub>2</sub>SO<sub>4</sub>. The membrane was then rinsed three times in lightly boiling water and stored in deionized water. The membranes were dried overnight in air in a covered Petri dish at room temperature. The MEA was formed by hot pressing the membrane between the painted anode GDE and a

woven carbon cloth cathode GDE (BASF LT250EWSI) cut into a 2.2 cm x 2.2 cm square, with 0.5 mg/cm<sup>2</sup> Pt/C (30 wt% Pt). The GDE/membrane sandwich was placed between two sheets of fiberglass-reinforced Teflon to prevent sticking and clamped between two flat aluminum plates. The assembly was put in a hot press preheated to 140°C, allowed to warm for 5 minutes, and then pressed for 2 minutes at 8.8 MPa. The assembly was removed and allowed to cool at room temperature for two hours before the MEA was separated from the FRT.

## **2.2 In Situ MEA Catalyst Processing**

### **2.2.1 MEA Test Fixture and Instrumentation**

Once the MEAs were assembled, a series of tests were performed to explore the behavior of PtSn catalysts under CO reformat conditions. PFA gaskets were cut to fit tightly around the anode and cathode GDE and extended beyond the Nafion membrane to form a tight seal when compressed. The MEA was aligned in a 5 cm<sup>2</sup> fuel cell test fixture from Fuel Cell Technologies (Los Alamos, NM), shown in **Figure 2.1**. Bolts lightly lubricated with thread lubricant were used to compress the test fixture to a total torque of 12 Nm with a torque wrench. The compressed test fixture was placed inside a fume hood to ensure safe ventilation of unused H<sub>2</sub> and CO gasses upon exit of the anode flow channel. All tests were conducted with a Scribner Associates (Southern Pines, NC) 850e fuel cell test stand that provides mass flow controllers, temperature controlled bottle humidifiers for both anode and cathode flow, cell temperature control, and an electronic load for changing operating voltage or current, all managed by Fuel Cell software.

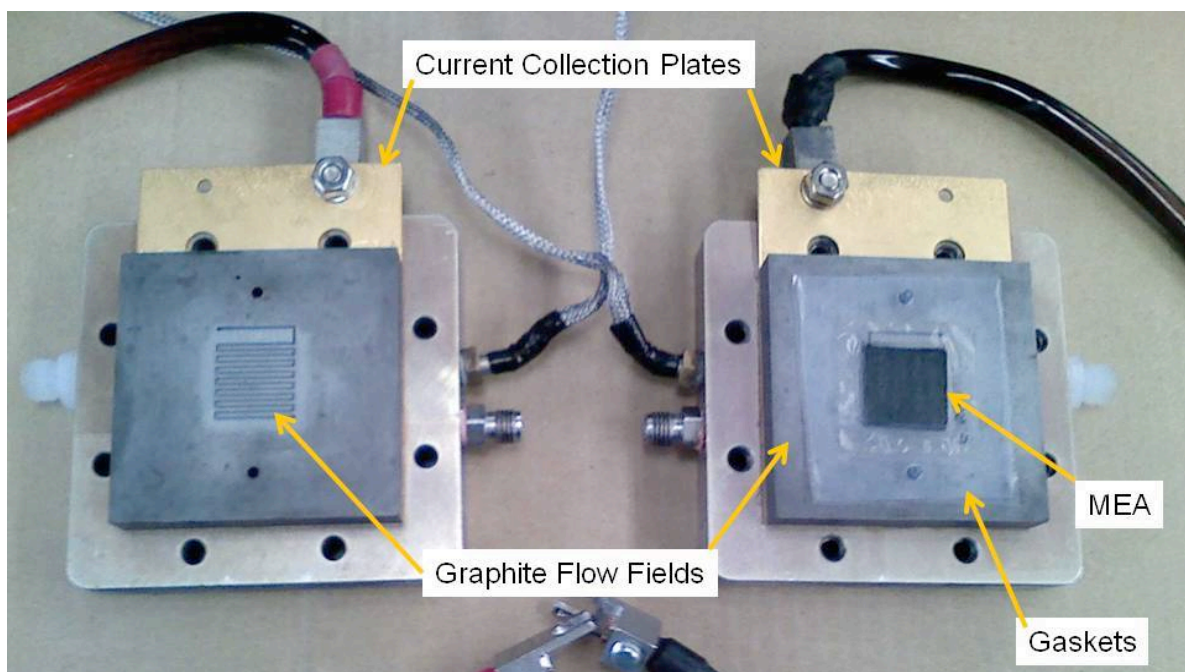


**Figure 2.1:** The single MEA test fixture showing the flow paths in the current collection plates and the MEA mounted onto one half of the test fixture.

For some of the anode catalyst processing via potential cycling, the load bank with the Scribner test stand was disconnected and an Autolab PGSTAT30 with 10 A current booster (EcoChemie, Netherlands) was used to control the anode and cathode voltages. This was done to drive the cell voltage past 0 V to negative voltages, a feature unavailable with the Scribner load bank, during potential cycling. Compressed bottled gases including breathing quality air for the cathode and ultra high purity H<sub>2</sub> (99.999% H<sub>2</sub> and CO + CO<sub>2</sub> < 1 ppm), CO, and 100 ppm and 1000 ppm CO mixtures in H<sub>2</sub> balance for the anode. The CO-containing mixtures were stored in aluminum bottles to avoid formation of volatile iron carbonyls with steel bottles, and the various mixtures were used to generate multiple CO concentrations in H<sub>2</sub> from 25 to 1000 ppm CO.

Various electrochemical characterization techniques were employed once testing had been completed. Polarization ( $V-i$ ) curves were obtained using linear sweep voltammetry (LSV) at various anode gas compositions. Stepwise increases in current were applied until a minimum cell voltage ( $V_{\text{cell}}$ ) was reached. Electrical impedance spectroscopy (EIS) measurements were also performed using various anode gas compositions by holding current constant and adding an AC current that changes from high frequency to low frequency.

### **2.2.2 Potential Cycling**

In the PtSn@Pt core shell RDE experiments, the core shell structure was created from a PtSn intermetallic catalyst by cycling the voltage in the presence of CO [32]. Potential cycling has been used in full cell MEAs to generate PtCu@Pt core shell cathode catalysts in both RDEs and MEAs [43, 44]. Potential cycling to change nanoparticle structure has been theoretically explored through DFT models [45]. DFT and Monte Carlo simulations have shown that adsorbates on the surface of an alloy can generate surface segregation of the alloy itself [46]. These studies suggest that potential cycling may be used on a PtSn intermetallic catalyst to drive CO oxidation, which may drive surface segregation and transform the catalyst into a PtSn@Pt core shell catalyst. This study attempted to achieve such catalyst transformations in a full MEA through the use of potential cycling and CO adsorption. The process should be optimized since excessive potential cycling can accelerate the degradation of an MEA by decreasing catalyst active surface area [49, 50]. Care should be taken to ensure that the cycling process keeps Sn particles from leaching out of the catalyst and migrating throughout the MEA. If allowed

to do so, Sn particles could interfere with either proton transport in the membrane or charge transfer in the cathode by blocking traditional pathways for each process.

A procedure for applying a cyclic potential to the anode for catalyst modification was developed in hopes of modifying the PtSn anode electrocatalysts as observed in potential cycling of the same catalysts in RDE experiments [32]. The RDE testing showed that after several hundred potential cycles from 0.0 V to 0.7 V (relative to a reversible H<sub>2</sub> electrode or -0.241 V to 0.459 V relative to a standard calomel electrode) in the presence of 1000 ppm CO in 1 M H<sub>2</sub>SO<sub>4</sub>, restructured the PtSn intermetallic nanoparticles into PtSn@Pt core-shell particles, which showed remarkably low overpotentials for CO oxidation [32]. The expectation was that the potential cycling in the MEA would duplicate the PtSn catalyst restructuring observed in the disk electrode experiments.

Several important differences exist for this process between the RDE experiment and the MEA experiment. The MEA has the PtSn/C intermetallic anode and a Pt/C cathode with separate gas flows whereas the RDE is a catalyst coated glassy disk electrode with a Pt wire as the counter electrode and a standard calomel electrode (SCE) as the electrode to which the voltage of the RDE is referenced. Since there is no reference electrode in the MEA setup, the cathode must be used as the reference as well as the counter electrode. This means that the voltages used in the RDE experiment will not directly correspond to the same voltages in the MEA, particularly when there are significant overpotentials associated with electrochemistry on the cathode. When air is used in the cathode flow, the cell voltages will include the cathode overpotentials. In the current study where the potential on the anode electrocatalyst is of interest to assess how

strongly these catalyst are being driven toward oxidation, it is important to subtract the overpotentials associated with the cathode and electrolyte membrane from the total voltage loss. One method for estimating those voltage losses for a particular MEA is to test the system with humidified H<sub>2</sub> on the anode side. Under such conditions at lower currents, the overpotentials associated with a well-designed Pt-based anode can be assumed to be relatively small. As such, the sum of overpotentials for a well-constructed MEA operating with humidified H<sub>2</sub> and a good anode catalyst layer can be approximated as the overpotentials associated with the cathode and electrolyte combined. The cathode overpotentials are associated with the O<sub>2</sub> reduction reaction and transport of gases to and from the channel flow through the cathode GDL to the catalyst layer. Voltage losses from the electrolyte membrane arise from transport of H<sup>+</sup> ions in the membrane. The estimated sum of cathode and electrolyte overpotentials increase with current density and these values can be subtracted from total overpotentials measured with CO-contaminated fuels to estimate effective anode overpotentials associated with the CO content,  $\eta_{CO}$ .

**Figure 2.2** shows an example of how CO overpotentials are determined in this study.

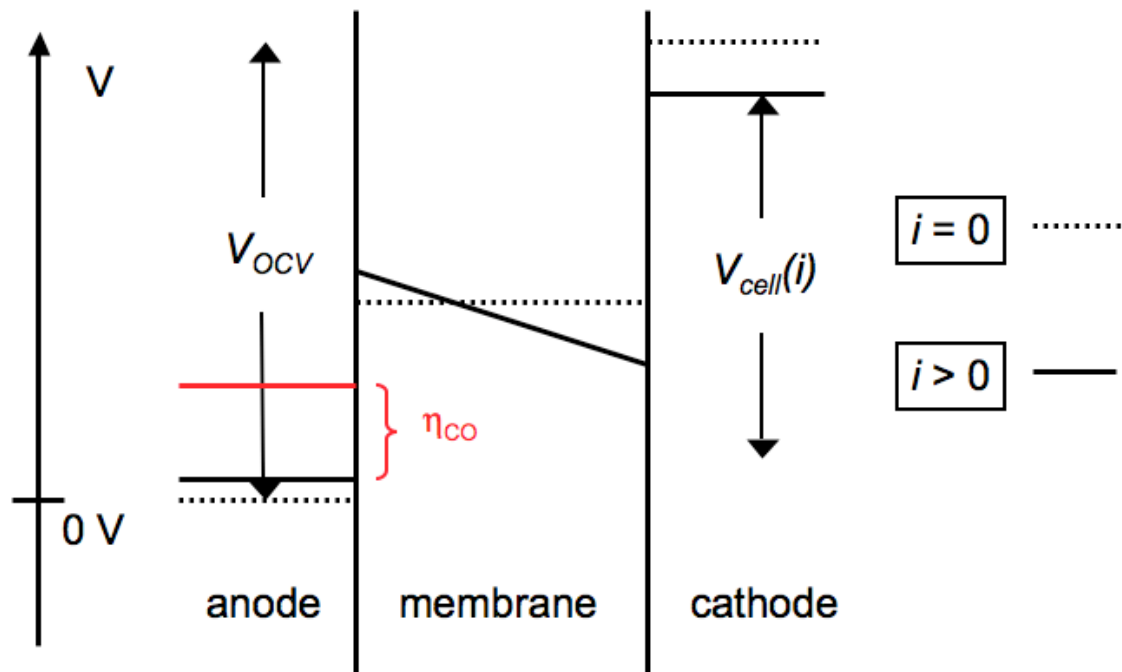


**Figure 2.2:** Distribution of potential relative to RHE across a PEMFC MEA showing how  $V_{cell}$  decreases from  $V_{OCV}$  as current is applied and again as CO is added to the anode

Cathode overpotentials are not seen in RDE experiments where the Pt wire counter electrode requires no gas adsorption process and both electrodes are submerged in a liquid electrolyte. The change in applied cell bias ( $V_{cell}$ ) during an attempted cycle will have contributions from both the anode and cathode sides of the MEA. Efforts to minimize the contribution of the cathode side would result in a process more closely resembling the RDE procedure.

The RDE potential cycling procedure used an  $\text{H}_2\text{SO}_4$  electrolyte solution at room temperature whereas a Nafion electrolyte membrane at  $70^\circ\text{C}$  separates the MEA electrodes. The electrolytes are of different phases and use different methods of proton transport, which may influence the effect of potential cycling on the catalyst in each application. In the RDE experiment, CO is bubbled through the liquid electrolyte

whereas the MEA has CO flowing through the anode channel along with a cathode channel containing a chosen gas composition. The choice of the cathode gas may change the effect that the presence of CO is having on the anode catalyst during potential cycling. The operating parameters of the MEA potential cycling experiment, shown in **Table 2.1**, were chosen to best mirror the conditions in the successful RDE experiment [32]. The potential cycling procedure was performed in sets of 200 or 400 cycles at a time, after which the MEA was tested for polarization data and EIS under standard operating conditions detailed in Section 2.3. The potential cycling procedure was repeated until improvement in polarization data ceased for both pure H<sub>2</sub> and CO containing anode fuel flows. The electronic load of the Scribner was originally used to perform the processing CO cycling procedure. The Autolab was used for both H<sub>2</sub> cathode gas cycling experiments and some air cathode gas cycling experiments for detailed voltage-current data. MEA 8a and 8b were cycled with identical gas composition and humidity settings. The 8a procedure used the Scribner electronic load for cycling over a smaller voltage range whereas the 8b procedure used the Autolab potentiostat to reach negative cell voltages.

**Table 2.1:** CO potential cycling operating conditions

Pressure	2 barg
Temperature	70°C
Anode Flow Rate	0.056 to 0.1 SLPM
Cathode Flow Rate	0.1 to 0.15 SLPM
Voltage Scan Rate	100 mV/s
Cycle Set Size	200 or 400
Cathode Gas	Air

The parameters involved in the potential cycling procedure were kept constant throughout all experiments. Other operating parameters were varied to observe their effect on both the cycling process and the final results. Similar processes have only been attempted in a full PEM fuel cell MEA for cathode catalysts without varying gas composition [43, 44, 45]. While many operating parameters can influence the potential cycling procedure toward higher CO tolerance in PEM fuel cell applications, the number of experiments was limited due to the extended time of the process from catalyst formation to termination of testing and the desire to conserve catalyst and MEA fabrication resources. Number of cycles per set, gas composition, and potential cycling range were parameters deemed most likely to be influential in transforming the PtSn intermetallic to the core shell PtSn@Pt structure in the anode catalyst. The results were compared to the results from a MEA using a PtRu anode electrocatalyst and results from PtSn research performed by other groups.

Gas composition was the factor deemed most likely to influence structural transformation of PtSn during potential cycling and was explored in such a way as to account for multiple different combinations of gases present and the ratio of those gases. The gas composition was varied since the partial pressure of CO bubbling through H<sub>2</sub>SO<sub>4</sub> solution in the RDE experiment that this experiment attempted to match is difficult to quantify. Using Henry's law of gas solubility, the partial pressure of CO is determined to be 0.0185 atm. It remains unclear whether the activity of H<sup>+</sup> in the H<sub>2</sub>SO<sub>4</sub> solution of the RDE experiments resembles that of H<sup>+</sup> in the membrane, which is difficult to quantify. Multiple CO to H<sub>2</sub>O ratios in the anode gas were explored since the CO oxidation reaction requires H<sub>2</sub>O as a reactant. The presence of H<sub>2</sub>O results in the formation of OH

ions on the catalyst surface, which are considered essential in the oxidation of CO off of a Pt catalyst site as indicated by Reactions 1.6 and 1.7 [52, 53]. Increasing the ratio would likely decrease the ability of CO to oxidize during the potential cycling process while decreasing the ratio would provide an excess of adsorbed OH to oxidize absorbed CO. The humidity of the anode gas flow was not decreased from the amount at normal operating conditions because doing so could influence the proton transport properties of the membrane, an effect not studied here. Humidifier dew points were increased to provide higher H<sub>2</sub>O fractions in the gas streams. The gas compositions used are listed by MEA in **Table 2.2**. MEAs with the same number in the label are from the same batch of catalyst as fabricated, arranged in chronological order. Separate letters of MEAs with the same number refer to the chronological order of hot pressing the painted anode GDE, cathode GDE, and membrane together. Water percentage was determined from the anode and cathode dew point temperature by assuming that the gas flows were saturated at the operating pressure of the cell. At larger potential cycling amplitudes, larger quantities of both CO and water are necessary to ensure that the anode stoichiometry is significantly above 1.0 to avoid transport losses. The stoichiometric ratios of both CO and H<sub>2</sub>O at 1 A are shown in **Table 2.3**.

**Table 2.2:** Anode gas composition by MEA, by percentage

MEA	CO	H <sub>2</sub> O	N <sub>2</sub>	H <sub>2</sub>
4b	0.1%	10.1%	0.0%	89.8%
5b	10.0%	15.4%	74.7%	0.0%
7a and 7b	1.8%	10.1%	0.0%	88.1%
8a and 8b	9.0%	10.1%	80.9%	0.0%
9c	89.9%	10.1%	0.0%	0.0%

**Table 2.3:** Stoichiometric ratio by MEA, calculated at 1 A

MEA	CO Stoich Ratio	Max Current (A)	H <sub>2</sub> O to CO
4b	0.02	0.44	101
5b	180	0.05	1.5
7a and 7b	0.29	1.01	5.6
8a and 8b	1.42	1.07	1.1
9c	4.70	2.14	0.1

Cycling potential range was varied in this study. It is difficult to equate the voltage range used during the RDE potential cycling experiments to cell voltages in a full MEA since changes in voltage with current density will occur on both the anode and cathode. In the presence of CO, an additional overpotential ( $\eta_{\text{CO}}$ ) occurs that can be estimated by assuming that the overpotentials that occur with pure H<sub>2</sub> represent the cathode and bulk overpotentials ( $\eta_{\text{cathode}}$ ,  $\eta_{\text{bulk}}$ ). A larger voltage range than the RDE experiment was implemented to account for the fact that the voltage includes these cathode and electrolyte overpotentials. Changing the cycling potential range can impact potential electrocatalyst structure transformations. The voltage must be driven low enough such that the anode potential rises to high enough values to promote CO oxidation. This shift in current corresponds with CO oxidizing off of the catalyst surface. The further the potential cycle proceeds before returning to OCV, the higher the currents arising from CO oxidation. CO oxidation likely has a significant role in formation of PtSn@Pt nanoparticles using the potential cycling method. Lower limits for  $V_{\text{cell}}$  during potential cycling varied from +0.2 V down to -0.3 V. OCV values varied for each test depending upon gas compositions and the amount of cycling already performed. The final OCV for each MEA at the end of cycling and minimum voltages during cycling are

shown in **Table 2.4**. All ranges provided adequately high anode voltages to ensure that CO oxidation occurs for the PtSn intermetallics and or core-shell PtSn@Pt catalysts. The CO tolerance depends on whether the cycling potential resulted in a large enough difference in anode voltage to force CO oxidation.

**Table 2.4:** Final OCV during CO cycling and cycling limit in V, by MEA

MEA	Cycling OCV	Cycle Limit
4b	-0.005	0.4
5b	0.377	-0.2 or -0.1
7a	0.896	0.0
7b	0.938	0.0
8a	0.648	0.2 or 0.0
8b	0.665	-0.3 or -0.2
9c	0.714	0.0

Using H<sub>2</sub> as the cathode gas as in MEA 4b to isolate the anode during the potential cycling process was attempted with hopes of isolating the potential cycling effect to the anode side. Starting with a potential range of OCV of 0 V, the voltage of the anode was increased relative to the cathode until significant currents from CO oxidation occurred. Although successful in implementation, the procedure resulted in a less active anode catalyst, as will be seen in Chapter 3.

The number of cycles between MEA electrochemical characterizations was also examined during the potential cycling tests. Voltage-current relationship during CO cycling is not constant, but instead varies as the number of cycles is increased. That relationship is indicative of the electrochemical behavior of the catalyst in the presence of CO. By increasing the number of cycles in a set, the degree to which that behavior is

changed is increased as well. It was clear at the beginning of testing that the total number of cycles to which an MEA is subjected affects the behavior of the catalyst. It was unclear whether or not the effect of switching back and forth between CO cycling and normal operation had any permanent effect on the progression of the CO tolerance of the anode catalyst under normal operation. Changing the amount of cycles per set examined this possibility.

## **2.3 MEA Characterization**

### **2.3.1 Electrochemical Characterization**

Polarization measurements record voltage as a function of current (or current density  $A/cm^2$  of membrane) in a fuel cell MEA. When plotted on a current density basis, the resulting  $V-i$  curve can be compared to MEAs with other catalyst layers, humidities, cell temperatures, gas compositions, or any other operating parameters of interest. For this study, polarization measurements were taken to track loss of cell voltage with increasing CO concentration, which is an effective standard of the MEA's CO tolerance. The CO overpotential is calculated as the voltage difference observed in an MEA as a function of current between anode flows containing pure  $H_2$  and some amount of CO. Polarization data was taken by starting at open circuit where  $I = 0$  A and increasing the current in steps of either 0.1 A every 10 seconds or 0.25 A every 20 seconds until the voltage drops below 0.4 V. The smaller step run accurately measures the activation region of the  $V-i$  curve whereas the larger step run accurately measures the ohmic and transport loss regions of the  $V-i$  curve. Polarization data was taken for pure  $H_2$

and 25 ppm CO anode flows after each set of cycling and for flows containing up to 1000 ppm CO after all cycling had been completed.

Electrical impedance spectroscopy (EIS) measurements can provide valuable information about PEM fuel cell MEAs. Galvanostatic EIS experiments are performed by holding the current constant, applying small changes to the current harmonically at a range of frequencies, and observing the voltage response. At high frequencies, the bulk impedance ( $R_{\text{bulk}}$ ) of the membrane dominates because it acts alone as a resistor without the catalyst-membrane interfaces being able to build a separation of charge. At low frequencies, the impedances associated with the anode oxidation reactions and the cathode O<sub>2</sub> reduction reactions at the catalyst-membrane interfaces contribute significantly to the total resistance. These impedances referred to as polarization resistance ( $R_{\text{pol}}$ ) increase with decreasing frequency because they act as a capacitive element by building a charge difference across the membrane. In normal operation, membrane and catalyst layer resistances can be determined from the Nyquist plot of the real and imaginary impedances by taking the high frequency and low frequency intercepts. Galvanostatic EIS measurements were taken at 100 and 500 mA/cm<sup>2</sup> with an excitation signal that was 5% of the DC amplitude with pure H<sub>2</sub> and 25 ppm CO anode flows after each set of cycling and at all CO concentrations during final characterization.

### **2.3.2 Ex situ Catalyst Characterization**

Scanning electron microscopy (SEM) was used to examine the structure of the anode catalyst layer. The catalyst layer is only tens of microns thick, making SEM ideal for taking high-resolution images. The images can be used to verify that the catalyst layer as painted is sufficiently uniform and devoid of any pinholes or cracking that could

occur during MEA hot-pressing. Energy-dispersive X-ray Spectroscopy (EDX or EDS), when combined with SEM imaging, provides information about the elemental composition of a sample. Different elements will produce a unique emission spectrum when bombarded with a focused X-ray beam. The complete emission spectrum can both determine what elements are present and the ratios of those elements. SEM and EDX analyses were performed at the University of Maryland's Nanoscale Imaging Spectroscopy and Properties Lab (NISP). An Ultra-High Resolution Hitachi SU-70 SEM machine was used to conduct SEM and EDX analyses. Samples were prepared for observation by SEM by freezing the MEA in liquid nitrogen and cracking it with a sharp blade to produce a clean cross section with minimal disruption of the structure of the catalyst layer. An example of a clean cross section is shown in **Figure 2.3** with different parts of the MEA labeled.

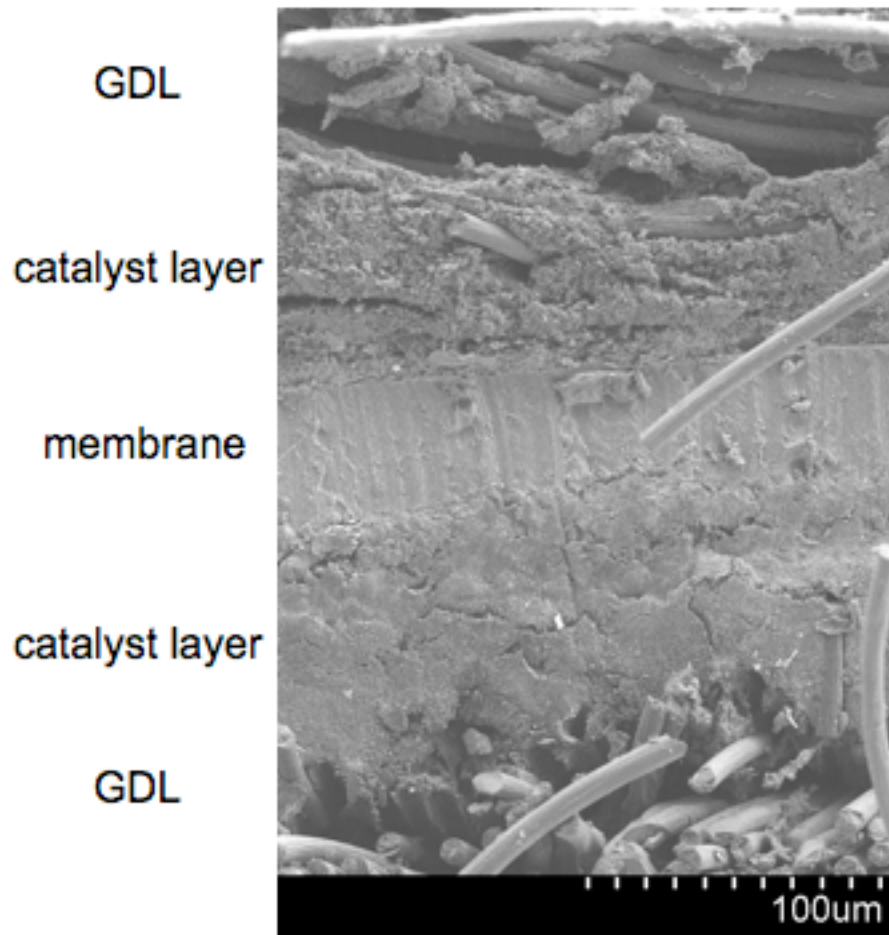


**Figure 2.3:** SEM image of MEA 4b after testing, 300X magnification

### 3 Electrochemical Results of Potential Cycled Anodes

The potential cycling process described above attempted to develop a CO tolerant, PtSn anode electrocatalyst in situ. By observing  $V$ - $i$  relationships both during potential cycling and under normal PEM fuel cell operating conditions, the CO tolerance of the resulting anode electrocatalyst was monitored as each experiment progressed. The data was compared between MEAs subjected to different cycling conditions to determine the effectiveness of operating conditions and potential cycling range and duration on anode electrocatalyst performance. EIS illuminates the relative impedances of independent processes occurring during PEM fuel cell operation with CO present and provides information about CO tolerance mechanisms. The collection of electrochemical data for each MEA presents a complete picture of its final CO tolerance capability after going through potential cycling.

#### 3.1 Potential Cycling for In Situ Electrocatalyst Modification

The MEAs tested and their total catalyst metal loadings after manufacturing were within  $\pm 0.05$  of  $0.5 \text{ mg/cm}^2$ , similar to previous CO tolerance studies [47]. The  $V$ - $i$  behavior of MEA 8b after cycling was similar to that of 8a during the initial stages of cycling, verifying that the Autolab and Scribner electronic load methods were sufficiently equivalent. A few of the MEAs were first exposed to  $\text{H}_2$  anode and air cathode gases under normal operating conditions ( $70^\circ\text{C}$  cell temperature and anode and cathode dew points with 2.0 barg back pressure) to establish a baseline  $V$ - $i$  curve before the cycling process. It was found that the OCV was lower than usual, 0.3 to 0.6 V compared to values of 0.9 or greater, and could not sustain current densities greater than  $20 \text{ mA/cm}^2$ .

Failing to establish a baseline set of data, the MEAs were immediately put through the potential cycling process, which slowly improved OCV and maximum allowable currents with increasing number of cycles. This increase in OCV and current may be explained by the restructuring of the PtSn intermetallic catalyst. While the PtSn is undergoing restructuring, surface Sn oxidation may be causing mixed potentials and suppressing rates for H<sub>2</sub> oxidation. As the surface is enriched with Pt during potential cycling, reversible H<sub>2</sub> oxidation becomes more likely for increased OCV and the improved surface activity allows for higher currents when a load is applied to the cell.

### **3.1.1 Variation of Cycles between Characterization**

CO cycling data was recorded in the form of current as a function of cell voltage. In RDE experiments, the potential of the RDE with PtSn intermetallic catalyst is raised by 0.7 V and lowered back to 0 V during the potential cycling process with respect to SCE, a fixed potential [32]. **Figure 3.1** shows that CO oxidation on a cycled PtSn intermetallic catalyst begins at a potential 0.1 V less than uncycled PtSn intermetallic, 0.15 V less than PtSn alloy and PtRu, and 0.25 V less than Pt [32]. This suggests that anode CO overpotentials of a PEMFC will be lower for a cycled PtSn intermetallic than for the other catalysts.

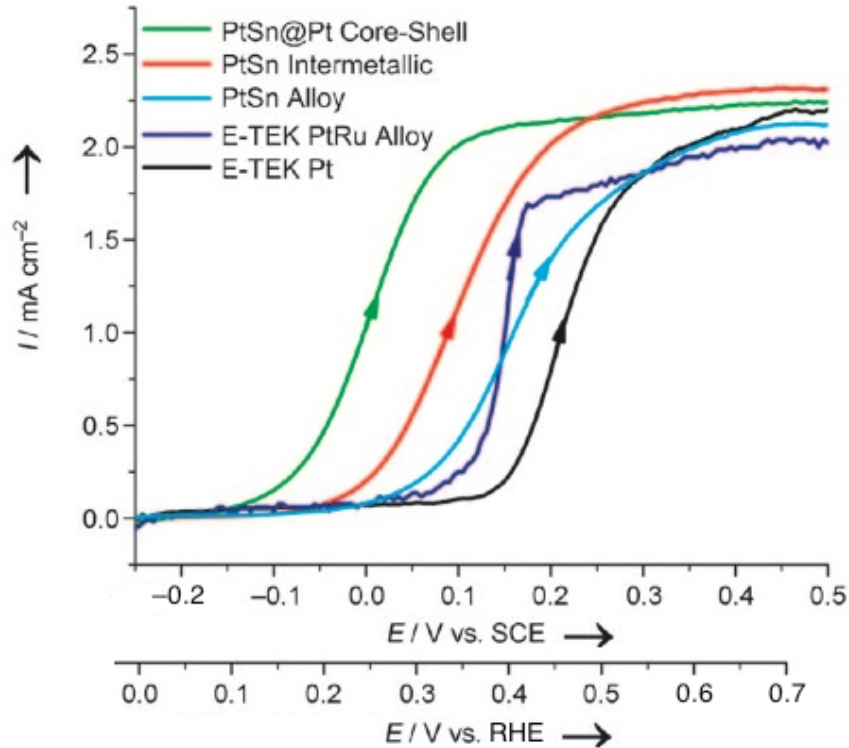


**Figure 3.1:** Polarization for CO oxidation using 1000 ppm CO using various anode electrocatalysts in RDE experiments: 298 K, 1mV/s scan rate, 1600 RPM, 0.5 M H<sub>2</sub>SO<sub>4</sub> electrolyte solution (taken from Liu et al. [32])

As mentioned previously,  $V_{\text{cell}}$  does not directly correspond to the voltage range in RDE experiments demonstrating CO oxidation. An approximation of anode voltage with respect to OCV during cycling can be determined. The cathode and bulk overpotentials combined are estimated from the cell voltage loss from OCV as a function of current for pure H<sub>2</sub> polarization anode feeds. This number is subtracted from  $\eta_{\text{CO}}$  to calculate the anode potential. Current as a function of both cell voltage and anode potential during cycling is shown in **Figure 3.2**. The curve shows an increase in current as the anode potential increases followed by a plateau at a fixed current. This is a mass transport limit

that occurs when reactants can no longer arrive at the catalyst fast enough to continue the CO oxidation reaction. Experiments where the CO overpotential cycling limit approaches 0.7 V more closely resemble the voltage cycling range in the RDE experiments.

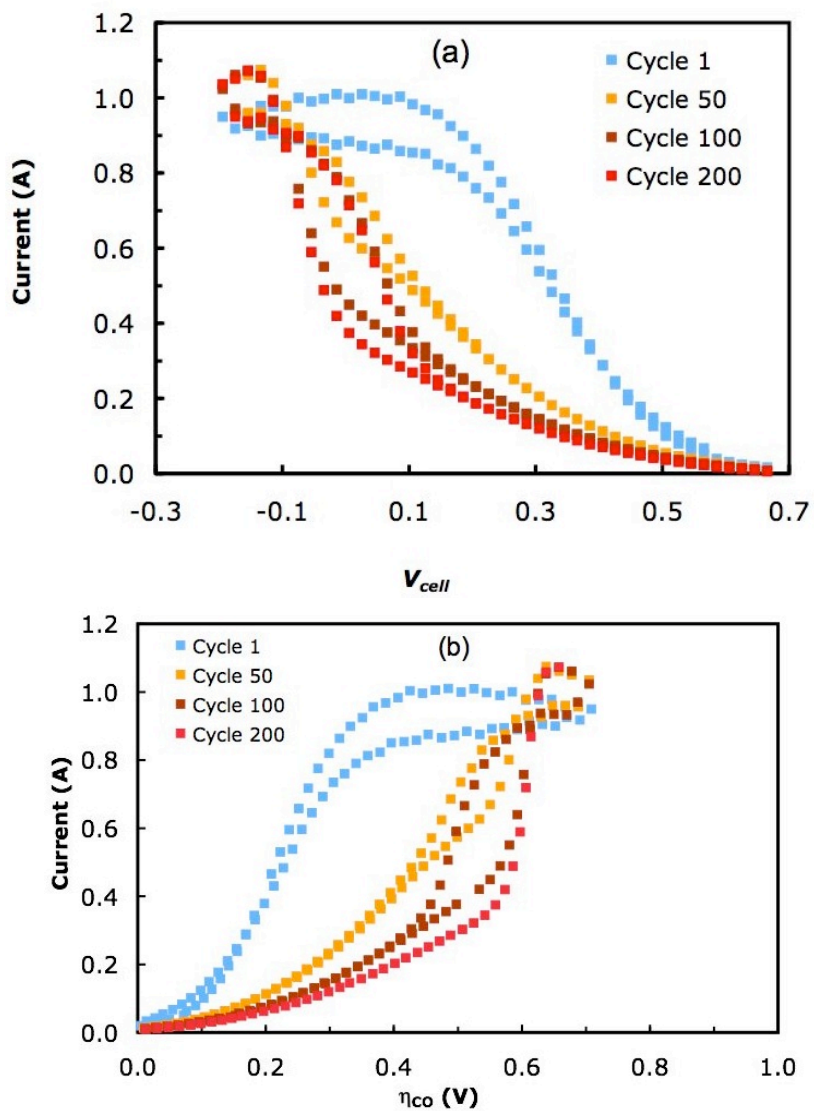


**Figure 3.2:** Current during potential cycle 1, 50, 100, and 200 of MEA 8b as a function of (a) cell voltage and (b) calculated anode potential. Cycles performed at 70 °C, OCV to -0.2 V cell potential range, 0.1/0.15 SLPM anode/cathode flow rates

Cycling data from MEA 8b shows that changing the cycling set size has very little effect on the final result. **Figure 3.3** shows a 400 cycle set (400 to 800 cycles overall) followed by a 200 cycle set (1000 overall) part-way through the potential cycling conditioning process of the anode catalyst layer. The first cycle shows the lowest onset potential of CO oxidation. As the number of cycles increases, the onset potential of CO oxidation shifts to higher potentials, eventually reaching an equilibrium. Most of the transformation of the cyclic voltammetry curve occurs during the first 50 to 100 cycles. The difference between the 200<sup>th</sup> and 400<sup>th</sup> cycle is miniscule in comparison to the transformation that occurs during the first 100 cycles. When cycling to modify the anode catalyst layer, a cycle set of 200 should be used since cycles 200 to 400 in an individual set have little effect and excessive cycling can degrade the MEA [49].

The number of cycles per set appeared to have no major effect on the catalyst conditioning process. MEAs 7a and 7b were both cycled with humidified CO and H<sub>2</sub> anode gas flow and air as the cathode gas. The anode gas mole fractions for each species were identical between 7a and 7b (see **Table 2.1**). MEA 7a was cycled in sets of 200 cycles with polarization and EIS data taken in between each set at standard operating conditions. MEA 7b was first cycled in a set of 800 and then cycled in two sets of 400. MEA 7a, with fewer cycles per set, reached a steady state performance at 0 ppm and 25 ppm in 800 total cycles. 7b reached a steady state after 1600 total cycles, but with only three overall cycling sets (800, 400, 400). The progression of polarization curves after each set of cycling followed virtually an identical pattern, shown in **Figure 3.4** and **Figure 3.5**. The *V-i* curves for pure H<sub>2</sub> and 25 ppm CO anode feeds shown in the next section were very similar. At the end of cycling, polarization curves showed that 7a and

7b reached current densities of 1000 and 1090 mA/cm<sup>2</sup> respectively at 0.6 V with pure H<sub>2</sub> anode gas and identical current densities of 360 mA/cm<sup>2</sup> at 0.6 V with 25 ppm CO.

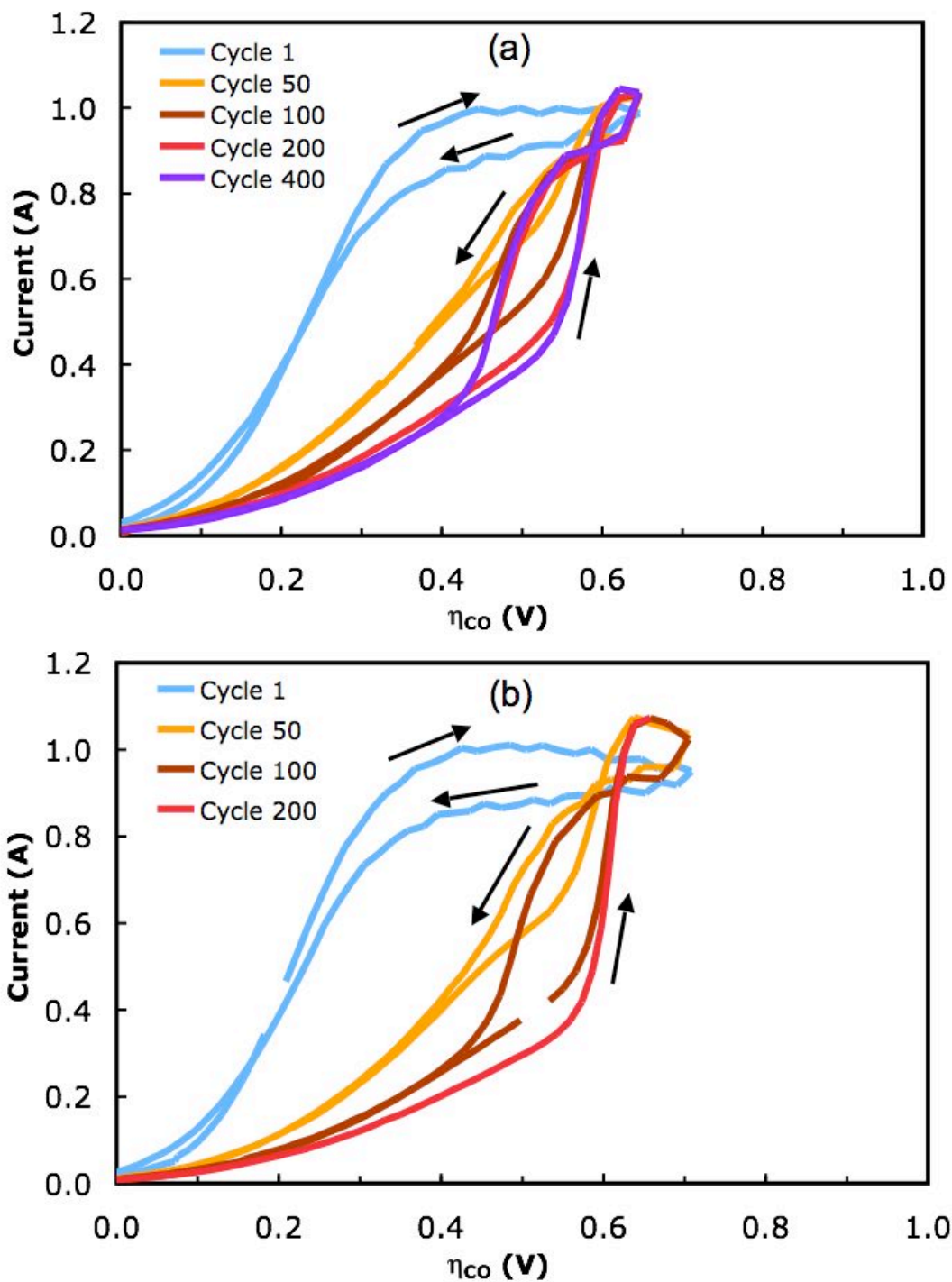


**Figure 3.3:** Effect of cycles between characterization, MEA 8b: (a) 400 cycles and (b) 200 cycles. Cycles performed at 70°C, OCV to -0.2 V potential range, 0.1/0.15 SLPM anode/cathode flow rates

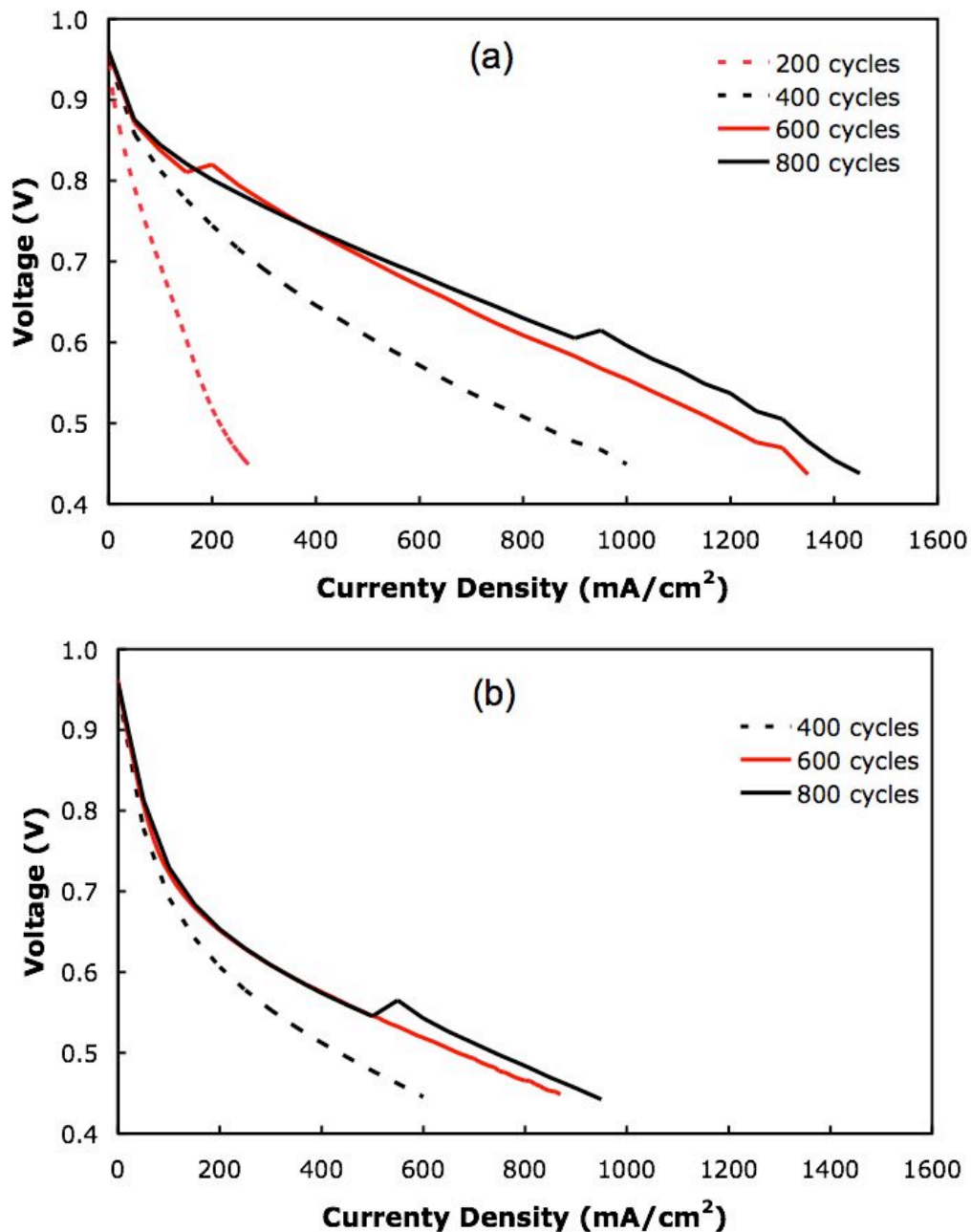


**Figure 3.4:** Comparison of cycle set size in post-cycling polarization of MEA 7a at 0 ppm (a) and 25 ppm (b) 2.2/2.2 stoichiometry with 0.56/0.133 SLPM minimum flow rates, 70 °C cell temperature with 70 °C anode and cathode dew points

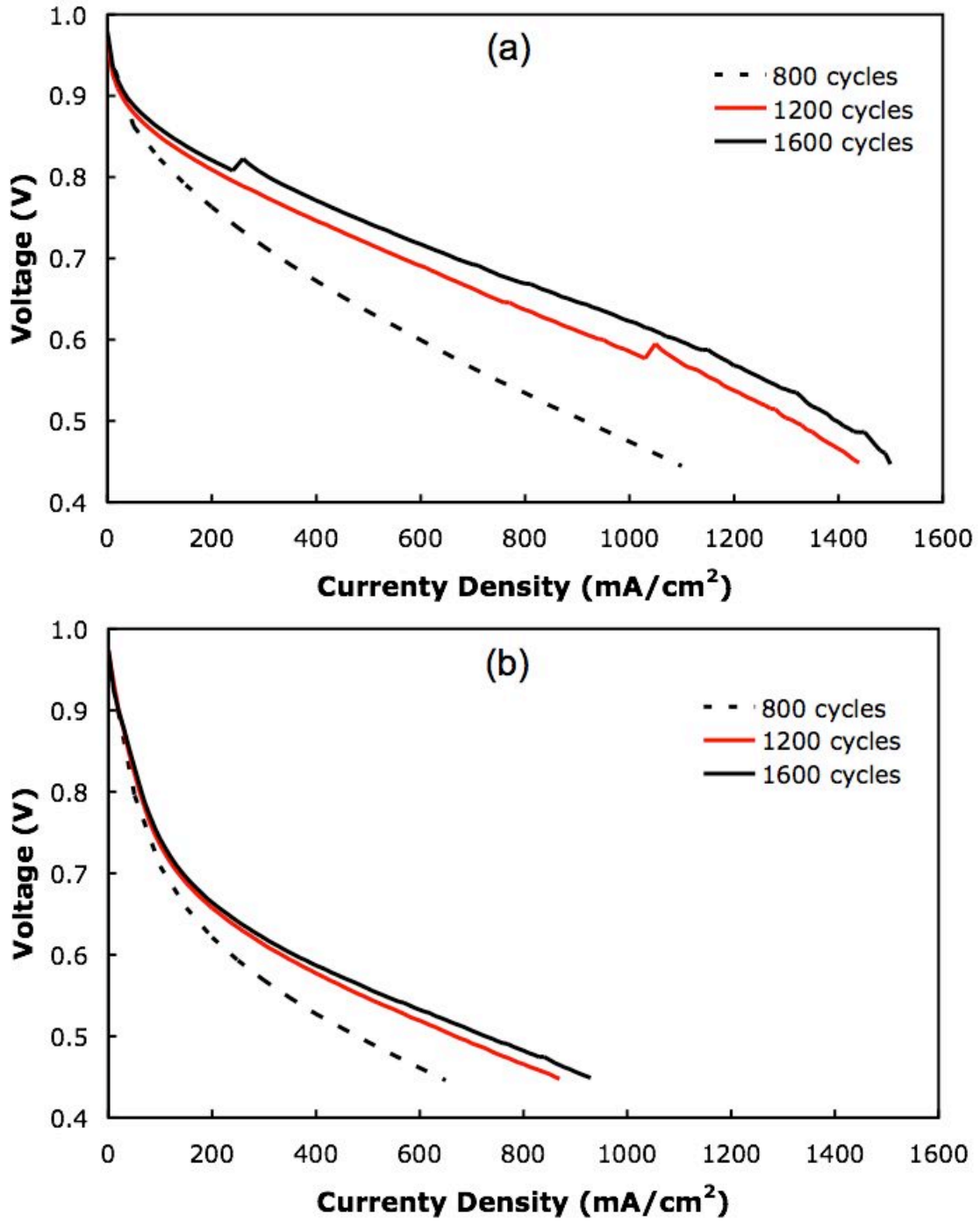


**Figure 3.5:** Comparison of cycle set size in post-cycling polarization of MEA 7b at 0 ppm (a) and 25 ppm (b): 2.2/2.2 stoichiometry with 0.56/0.133 SLPM minimum flow rates, 70 °C cell temperature with 70 °C anode and cathode dew points

### 3.1.2 Variation of Potential Cycling Range

Increasing the  $V_{\text{cell}}$  limit below 0 V during cycling appeared to hinder the catalyst conditioning process. MEAs 8a and 8b were both cycled using a humidified CO and H<sub>2</sub> anode gas flow using the same proportions with air as the cathode gas. MEA 8a was cycled using  $V_{\text{cell}}$  from OCV to 0 V whereas MEA 8b was cycled using  $V_{\text{cell}}$  from OCV to either -0.3 V or -0.2 V. Through the first 1000 cycles, **Figure 3.6** and **Figure 3.7** show that MEA 8a and 8b proceeded through similar progressions of successive post-cycling polarization curves. MEA 8a eventually exhibited higher currents. After 1000 cycles, pure H<sub>2</sub> anode gas polarization curves showed that 8a reached a current density of 1250 mA/cm<sup>2</sup> at 0.6 V whereas 8b only reached 810 mA/cm<sup>2</sup> at 0.6 V. With a 25 ppm CO anode gas composition, the shape of the polarization curves of 8a began to change to allow for higher currents at voltages above 0.8 V whereas the shape of the polarization curves of 8b did not change with increased cycling. The calculated  $\eta_{\text{CO}}$  remained below 0.05 V at up to 160 mA/cm<sup>2</sup> in 8a whereas  $\eta_{\text{CO}}$  for MEA 8b reached 0.05 V at 55 mA/cm<sup>2</sup>. Alternatively, 8b had a current density of 860 mA/cm<sup>2</sup> at  $V_{\text{cell}} = 0.45$  V compared to 8a with 750 mA/cm<sup>2</sup> using 25 ppm CO. Maintaining a lower voltage range promotes further changes in the anode catalyst layer, but whether this is a positive or a negative effect on CO tolerance is unclear and will be discussed in Section 3.2 and 3.3.

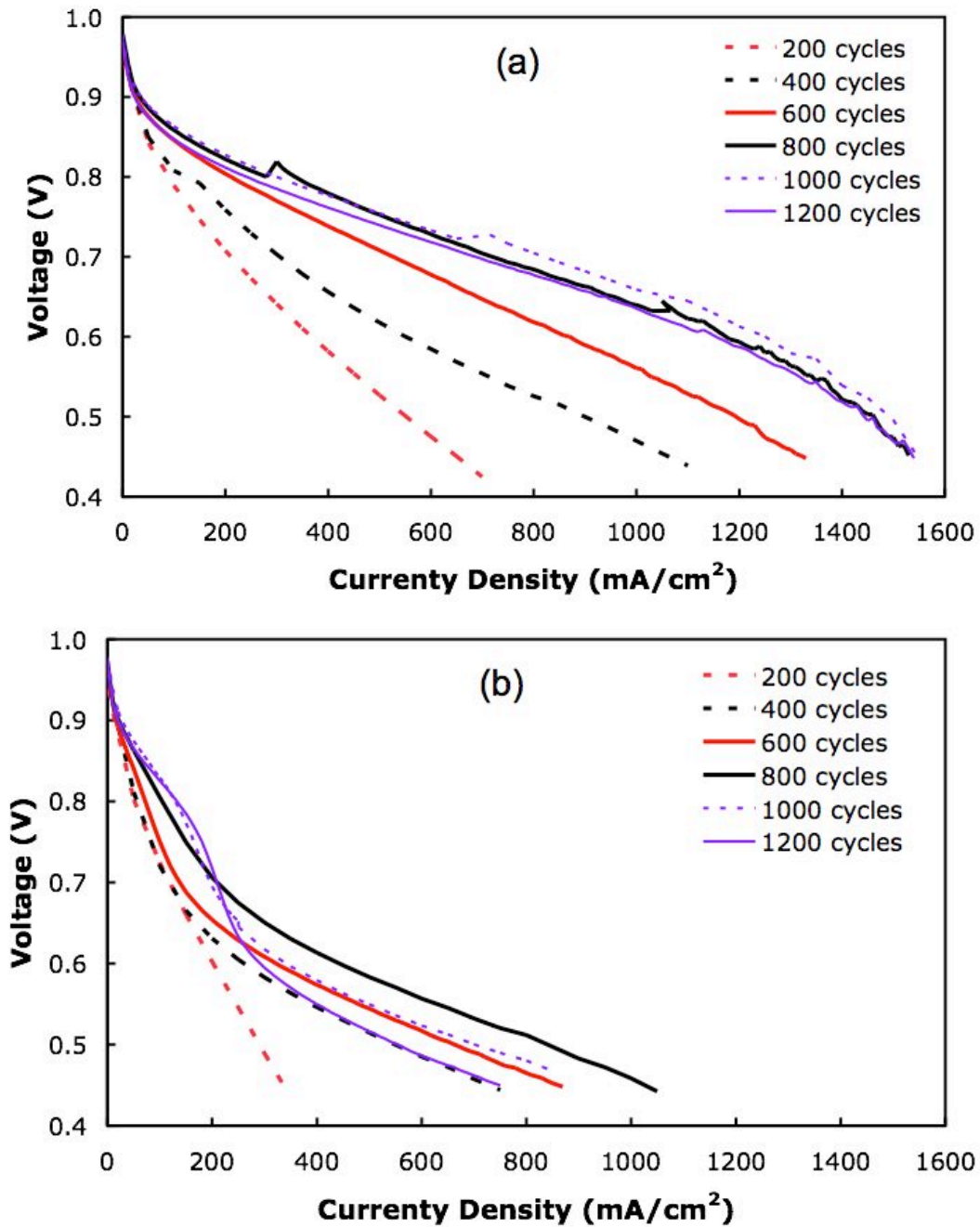


**Figure 3.6:** Comparison of cycle set size in post-cycling polarization of MEA 8a at 0 ppm (a) and 25 ppm (b): 2.2/2.2 stoichiometry with 0.56/0.133 SLPM minimum flow rates, 70 °C cell temperature with 70 °C anode and cathode dew points

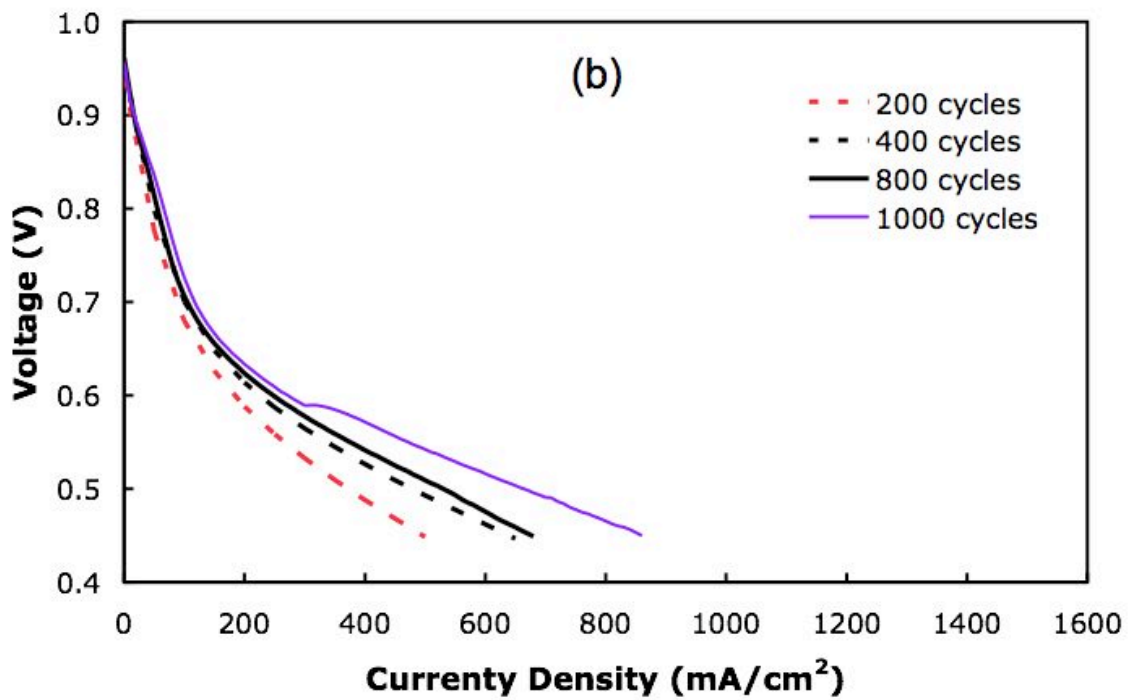
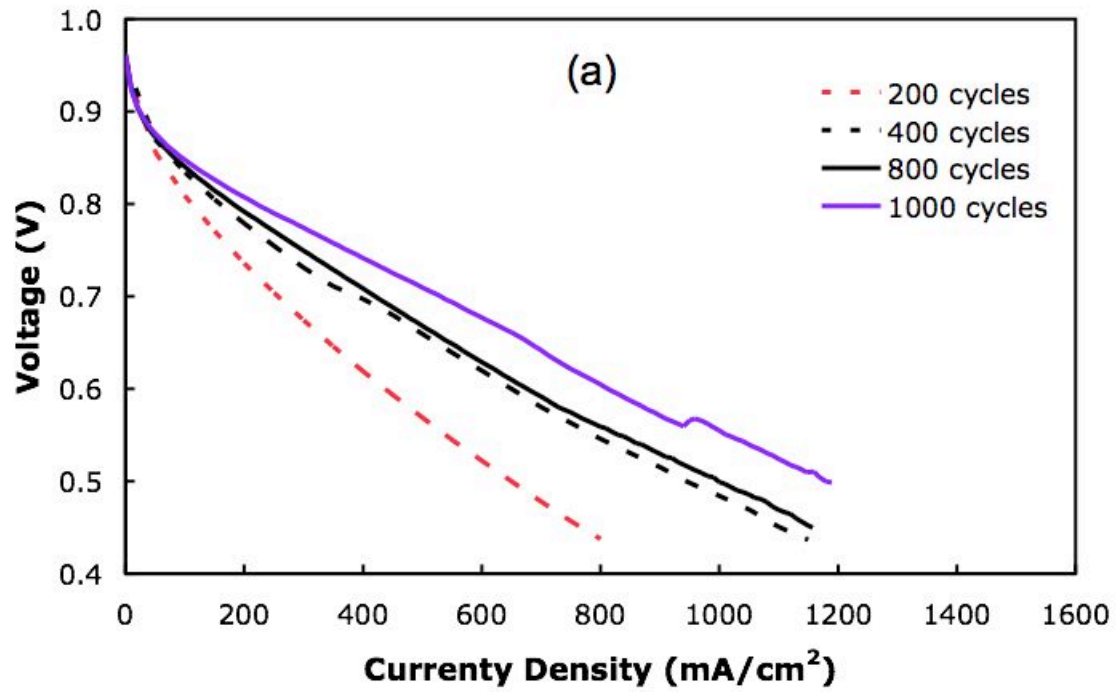


**Figure 3.7:** Comparison of cycle set size in post-cycling polarization of MEA 8a at 0 ppm (a) and 25 ppm (b): 2.2/2.2 stoichiometry with 0.56/0.133 SLPM minimum flow rates, 70 °C cell temperature with 70 °C anode and cathode dew points

### 3.1.3 Variation of Gas Composition

Five different anode gas compositions, detailed in **Table 2.2**, were used for the CO cycling process. CO and H<sub>2</sub>O were present and for some potential cycling studies the anode mixture was diluted with N<sub>2</sub> or H<sub>2</sub>. All cycling experiments used air as the cathode gas with the exception of 4b, which used a H<sub>2</sub> cathode flow.

H<sub>2</sub>O acts as the oxidant in the CO oxidation reaction, through Reaction 1.6 and also the source of H<sub>2</sub> and thus protons for Reaction 1.1 and 1.7. This implies that the amount of H<sub>2</sub>O available in the anode is critical to the CO oxidation process. Since the CO oxidation is deemed critical for anode catalyst restructuring [32], it is important variable to explore. The stoichiometric ratios calculated at a current of 1 A show that, for MEAs 4b and 7a/7b, there is a limited amount of CO to perform the reaction. MEAs 8a and 8b have just enough CO to execute CO oxidation and MEAs 5b and 9c have more than enough CO. Conditions for all experiments either had just enough H<sub>2</sub>O for CO oxidation or had H<sub>2</sub>O in excess, preventing H<sub>2</sub>O from being a limiting factor. The ratio of CO to H<sub>2</sub>O varied from very low values (4b and 7a/7b), intermediate values (5b and 8a/8b), and very large values with excess CO (9c). Cycling experiments with lower stoichiometric ratios run the risk of becoming mass transport limited as the cell voltage is lowered, meaning that the flow rates are not large enough to provide the reactants necessary to sustain the reaction at higher currents. These ratios have significance because many of the MEAs expressed peak currents of approximately 1 A during potential cycling.

The final two cycling sets from MEA 8b were shown previously in **Figure 3.3**. A voltage cycle starts at OCV (0 V overpotential), and decreases  $V_{cell}$  at a rate of 100 mV/s.

As it does so, the current remains near zero until a critical voltage is reached where the current increases dramatically and eventually establishes a linear voltage-current relationship. This critical voltage varies among MEAs. As  $V_{\text{cell}}$  decreases and the  $\phi_{\text{anode}}$  rises, the reaction reaches a point where there is insufficient gas transport to the anode to sustain the current, which results in a transport current limit. The voltage-current relationship shows hysteresis during cycling. Initially, the current is lower during the return to OCV. By the 50<sup>th</sup> cycle, current is higher during the return to OCV and remains that way for the remainder of cycles in the set. As the number of cycles increases, the slope of the linear voltage-current relationship decreases, shifting the body of the curve to the left. Ultimately, the  $V$ - $i$  relationship exhibits two different slopes: a shallow slope at the onset of CO oxidation and a steep slope when approaching the limit of the cycle. This progression is exhibited during each cycling set and the final shapes of the curves after each set are extremely similar for all sets not shown here.

CO cycling data from MEA 9c displaying the final cycling set is shown below in **Figure 3.8** using the CO overpotential method to estimate anode voltage. The initial lack of current and sharp current increase at the onset of CO oxidation is exhibited for these conditions just as it was for the conditions of MEA 8b. Unlike MEA 8b, 9c does not demonstrate a current plateau when approaching 0 V. A small amount of hysteresis is present in the first cycle compared to MEA 8b, but disappears as the number of cycles in the set increases.

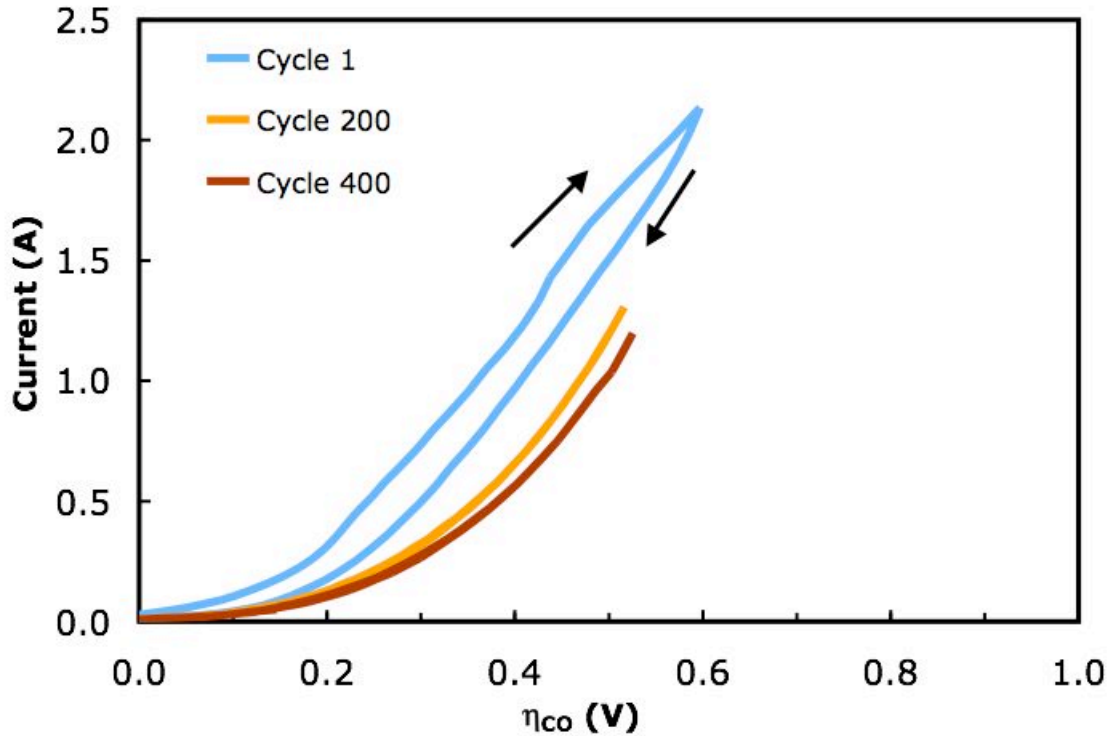


**Figure 3.8:** CO cycling procedure, first, 200<sup>th</sup>, and last cycle at end of cycling, MEA 9c.  
Cycles performed at 70°C, OCV to 0 V cell potential range, 0.34/0.15 SLPM  
anode/cathode flow rates

**Figure 3.9** shows the last cycle in each set for MEA 9c. For the first three sets, the current increases slightly as the number of cycles increases. The third set shows a jump in peak current by 0.5 A, after which all other cycling sets show a decline in current as each set progresses. A steady increase in current in the 400<sup>th</sup> cycle of the set is seen for the first four sets. In contrast, the final cycle in sets five through eight shows virtually no change. The initial peak current of the first cycle increases but eventually settles down to roughly 1.2 A. The stoichiometric ratios for both CO and H<sub>2</sub>O were large

enough to prevent mass transport effects from limiting the current at high anode potentials even though maximum currents of over 2A were reached in the final two sets.

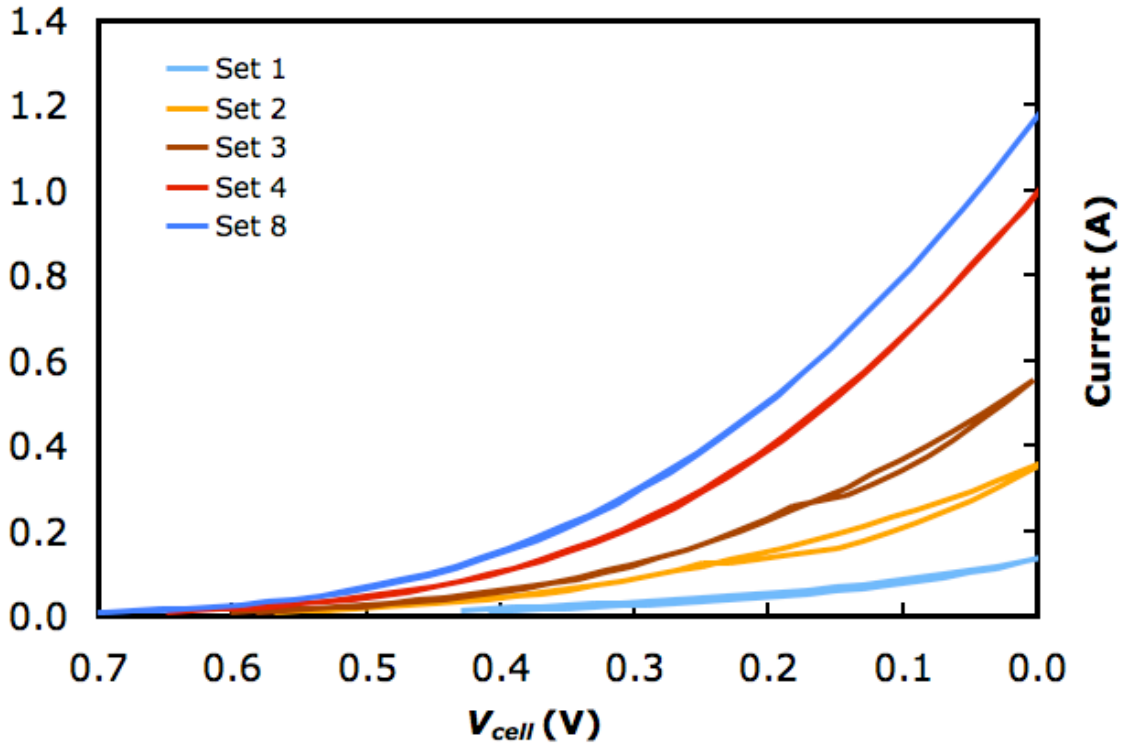


**Figure 3.9:** CO cycling procedure for MEA 9c, 400<sup>th</sup> and last cycle of each set for sets 1 through 4 and set 8. Cycles performed at 70°C, OCV to 0 V cell potential range, 0.34/0.15 SLPM anode/cathode flow rates

A cycling procedure was attempted with H<sub>2</sub> as the cathode gas and 1000 ppm CO in H<sub>2</sub> as the anode gas to try to isolate the effects of cycling to the anode without having any cathode overpotential contribution. The voltage of the anode was increased from OCV to 0.4 V using the cathode as the reference and counter electrode. The process is similar to decreasing the voltage from OCV using air as the cathode gas. Increasing the

anode voltage in a H<sub>2</sub> cathode gas cycling experiment with respect to the cathode is equivalent to decreasing the cell voltage in an air cathode gas cycling experiment.

**Figure 3.10** and **Figure 3.11** show cycling data from MEA 4b. The  $V-i$  relationship of the cycle with H<sub>2</sub> as the cathode gas behaves differently than the cycle with air as the cathode gas. Unlike tests with air over the cathode, current increases immediately and continues to increase up through 0.4 V. Hysteresis is evident in the current path as return path is higher than the upward path. As the number of cycles increases, the initial slope remains the same but the amount of hysteresis exhibited by the curve decreases. 200 cycles were performed in each set. In the first three sets of cycling, the shape of the curve does not change significantly after the first 25 cycles. The fourth cycling set showed a very large current on the first cycle that eventually settled back to previous levels at the end of the set (**Figure 3.10b**). Afterwards, current began to decrease with successive cycles in a set (**Figure 3.11a**). Observing the 100<sup>th</sup> cycle of each set in **Figure 3.11b**, the peak currents rose through sets one through four and decreased in set five. Cycling was stopped at this point to characterize the MEA electrochemically through polarization and EIS data.

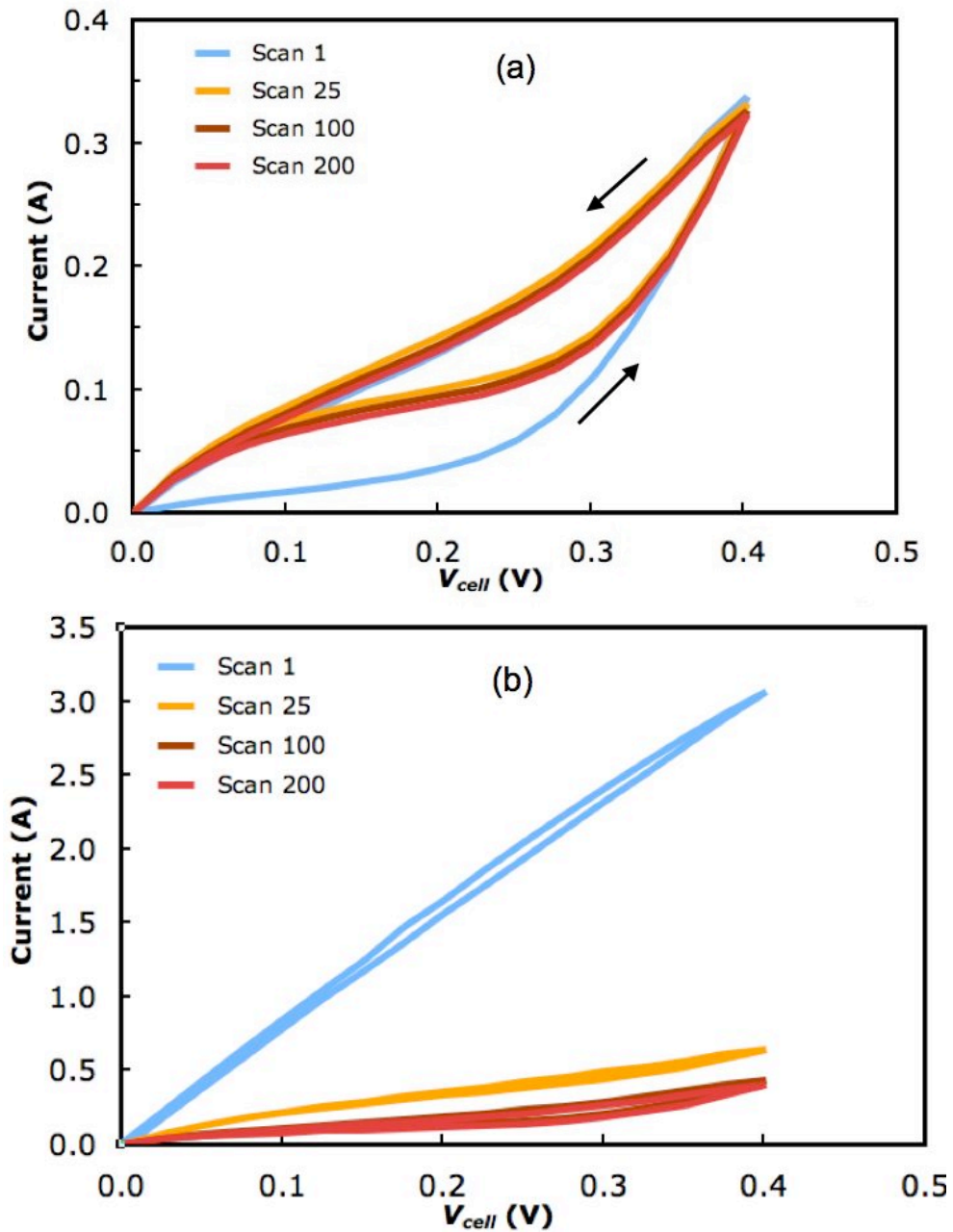


**Figure 3.10:** CO cycling procedure, MEA 4b (a) cycles 400 to 600 (b) cycles 600 to 800 with  $H_2$  cathode gas and 1000 ppm CO anode gas. Cycles performed at  $70^\circ C$ , OCV to 0.4 V cell potential range, 0.1/0.1 SLPM anode/cathode flow rates

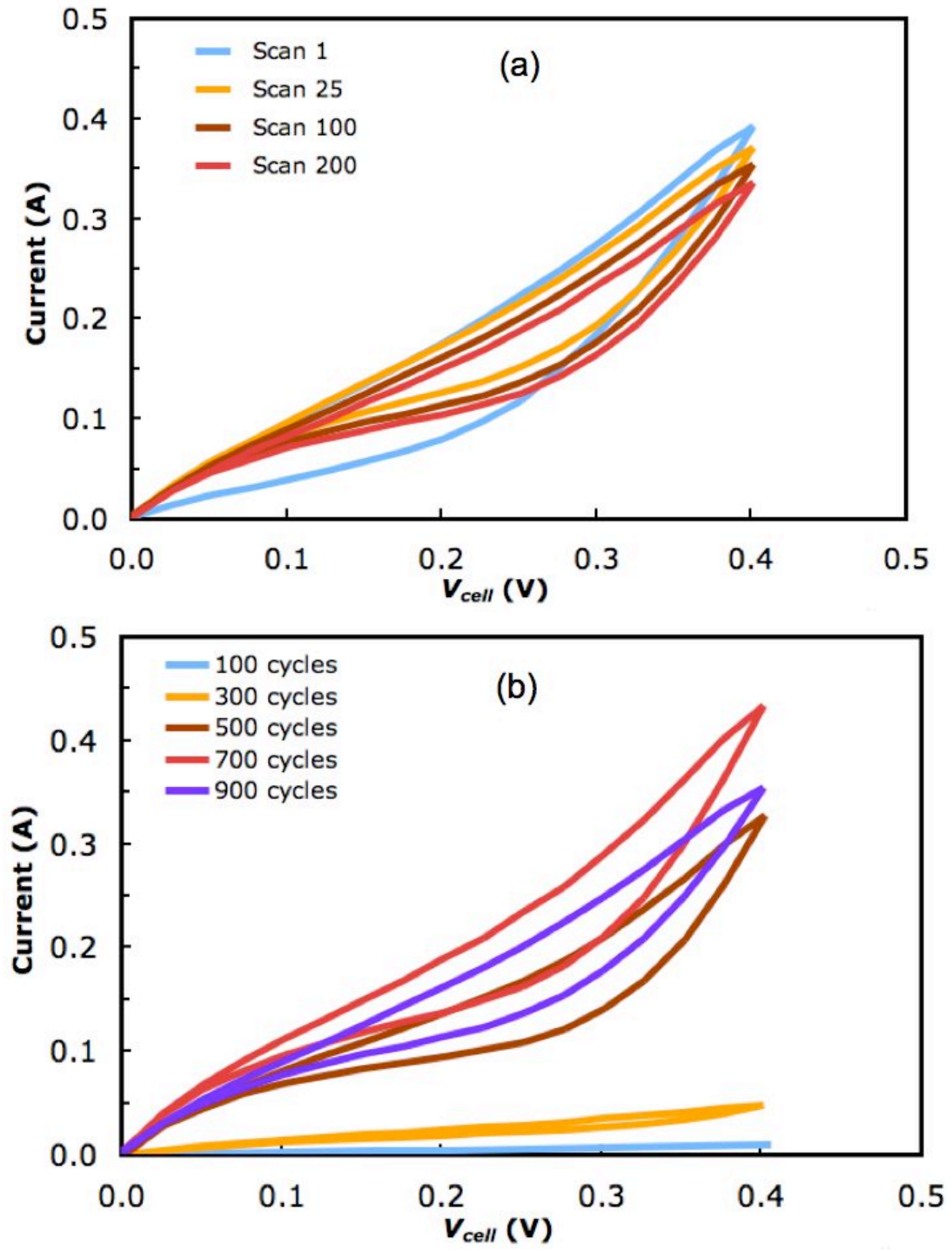


**Figure 3.11:** CO cycling procedure, MEA 4b (a) cycles 800 to 1000 (b) 100<sup>th</sup> cycle of each set with H<sub>2</sub> cathode gas and 1000 ppm CO anode gas. Cycles performed at 70°C, OCV to 0.4 V cell potential range, 0.1/0.1 SLPM anode/cathode flow rates

To determine if H<sub>2</sub> impacts the potential cycling process, experiments were performed with H<sub>2</sub> or N<sub>2</sub> as the balance gas during cycling. Exploring this factor helps determine if the interaction between H<sub>2</sub> and CO adsorption and oxidation causes the transformation to a improved CO tolerance PtSn@Pt anode catalyst. The presence or absence of H<sub>2</sub> may also play a role in the stability of the PtSn@Pt core shell nanoparticle once it is formed. **Figure 3.12** shows the CO cycling results from an MEA under the conditions of MEA 5b. A set of 200 cycles was performed with H<sub>2</sub> instead of N<sub>2</sub> as the balance gas. Afterwards, the balance gas was switched back to N<sub>2</sub> and 200 more cycles were performed. The first and last cycles of each set are displayed here. There is a small increase in current from the first to last cycle with H<sub>2</sub> as the balance gas between the first and last cycle. Slightly lower currents are observed with N<sub>2</sub> as the balance gas and no transformation is seen over the course of the 200 cycle set. The similarity in form and current values as a function of voltage between the two different balance gases suggests that it is the presence of CO that is dominating the cycling process and that the balance gas is of little importance.

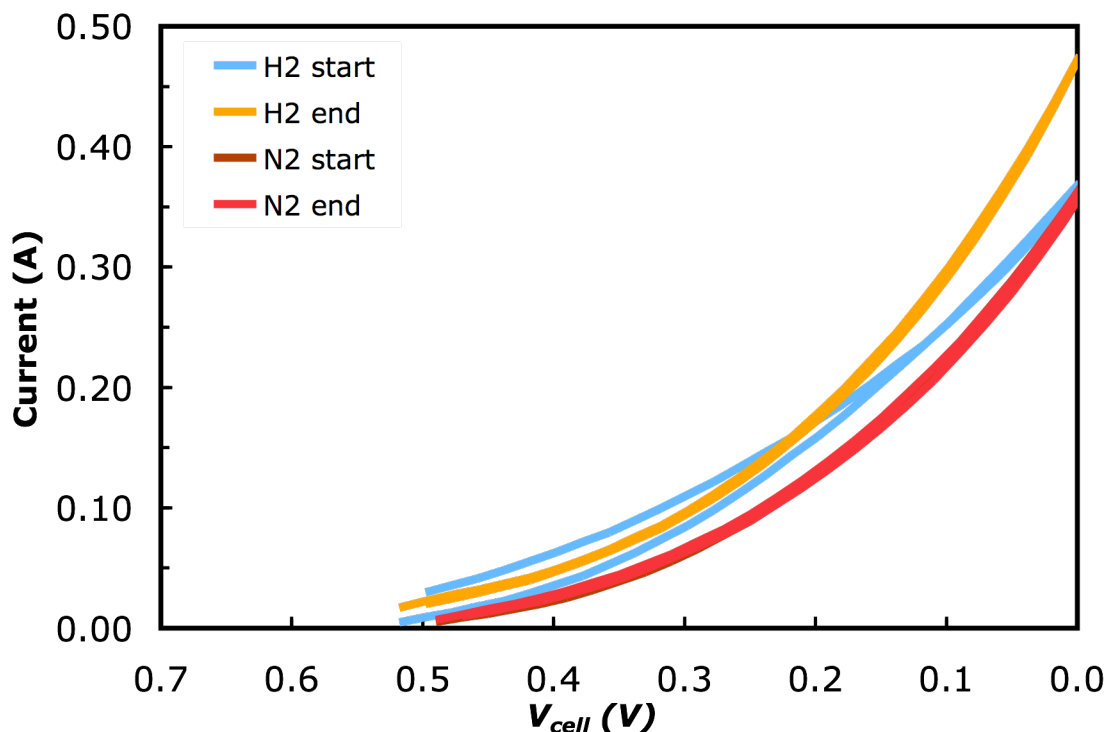


**Figure 3.12:** Balance gas comparison: 200 potential cycles with H<sub>2</sub> balance gas followed by 200 potential cycles with N<sub>2</sub> balance gas. Cycles performed at 70°C, OCV to 0.4 V cell potential range, 0.1/0.1 SLPM anode/cathode flow rates

## 3.2 Electrochemical Performance on CO-Laden Fuels

### 3.2.1 Polarization Curves

Polarization data for the complete set of cycled MEAs considered in this study are shown below in **Figure 3.13**, **Figure 3.14**, and **Figure 3.15**. With the exception of 5b, all cycling procedures produced an MEA that exhibited an OCV of greater than 0.9 and a current density of at least 1000mA/cm<sup>2</sup> at 0.5 V. The general form of the polarization

curves as CO concentration increases follow a similar pattern across all MEAs. All polarization curves with a CO containing anode flow demonstrate a steep drop in voltage before reaching 200 mA/cm<sup>2</sup>. After the drop, the slope of the  $V-i$  curve which is equivalent to the area-specific-resistance (ASR) becoming roughly parallel with the slope of the pure H<sub>2</sub> polarization curve. The onset of a large  $\eta_{\text{CO}}$  in MEA 8a occurs at slightly higher currents than the rest of the MEAs outside the activation region and in the ohmic region of the polarization curve. This results in higher currents at voltages greater than 0.8 V but lower currents at voltages less than 0.6 V. It was thought that polarization data from MEA 8a represented an intermediate stage in the transition of the anode catalyst from a CO poisoned state to a more CO tolerant state, but successive cycling first did not improve and then caused degradation in the polarization data.

The CO overpotential of MEA 8a shows a low CO overpotential until 200 mA/cm<sup>2</sup>, where a dramatic rise occurs followed by a return to a slow increase in CO overpotential above 400 mA/cm<sup>2</sup>. MEA 7a, 7b, and 8b show an immediate dramatic increase in CO overpotential followed by a return to slow increases at 200 mA/cm<sup>2</sup>. Eventually, CO overpotential remains constant as a function of current at higher current densities for these three MEAs. CO overpotentials for 7a, 7b and 8b at higher current densities are less than 8a, reflecting the fact that pure H<sub>2</sub> polarization results for MEA 8a had lower cathode and bulk overpotentials than the other three. Current as a function of voltage for all four MEAs are roughly equivalent through 100 PPM.

The MEA with PtRu(1:1.5) anode catalyst shown in **Figure 1.3** exhibits higher currents with pure H<sub>2</sub> (1400 mA/cm<sup>2</sup> at 0.6 V) and large improvements in current at CO concentrations up to 1000 ppm. The PtRu MEA does not see an instantaneous drop in

voltage due to CO, but instead CO overpotential slowly increases as current increases.

Only at voltages less than 0.5 V with higher CO concentrations used does PtSn data from

7a and 7b begin to match the PtRu catalyst in current density.

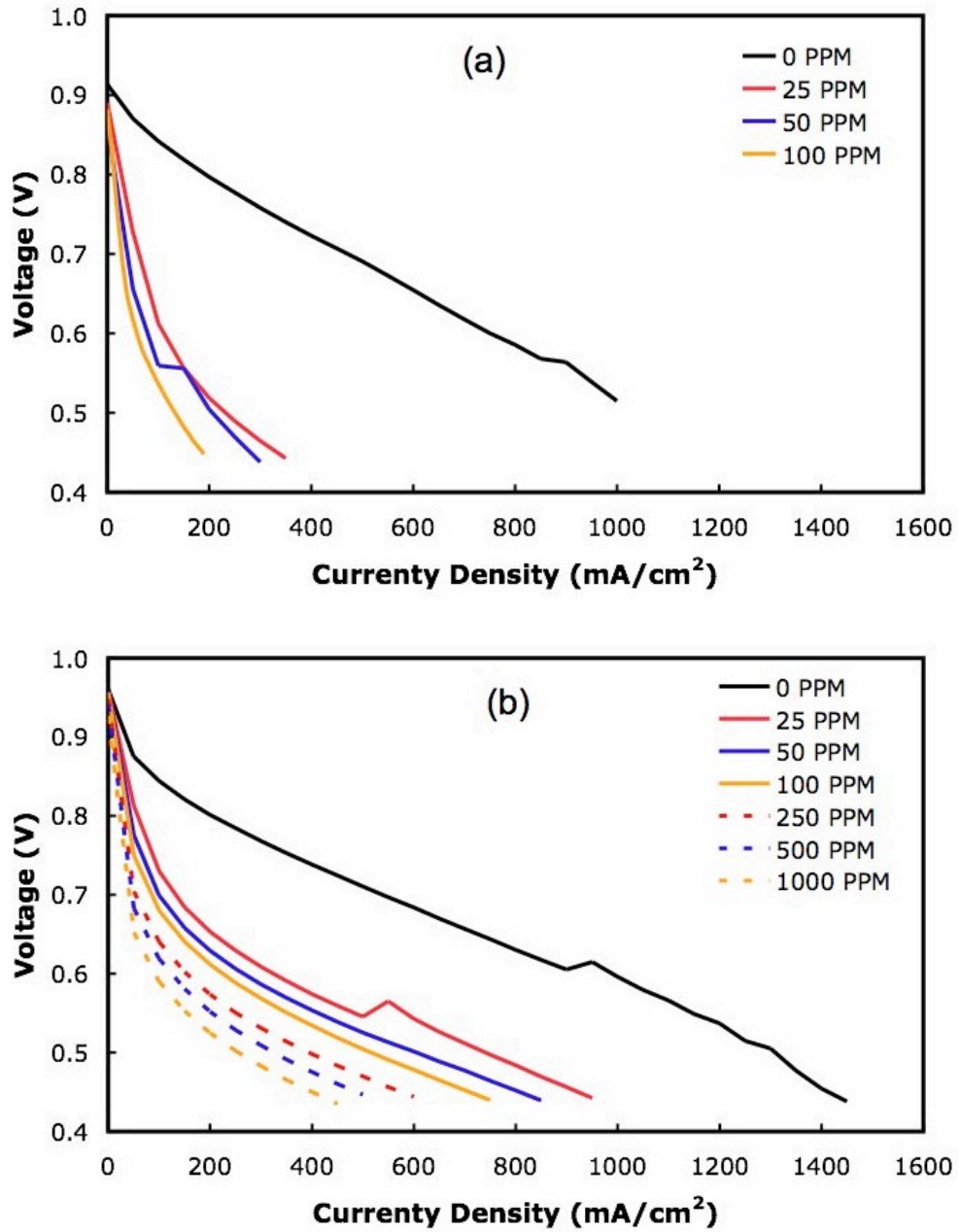


**Figure 3.13:** Polarization data of MEA (a) 4b and (b) 7a, potential cycled PtSn anode catalyst with up to 1000 PPM CO. 2.2/2.2 stoichiometry with 0.56/0.133 SLPM minimum flow rates, 70 °C cell temperature with 70 °C anode and cathode dew points

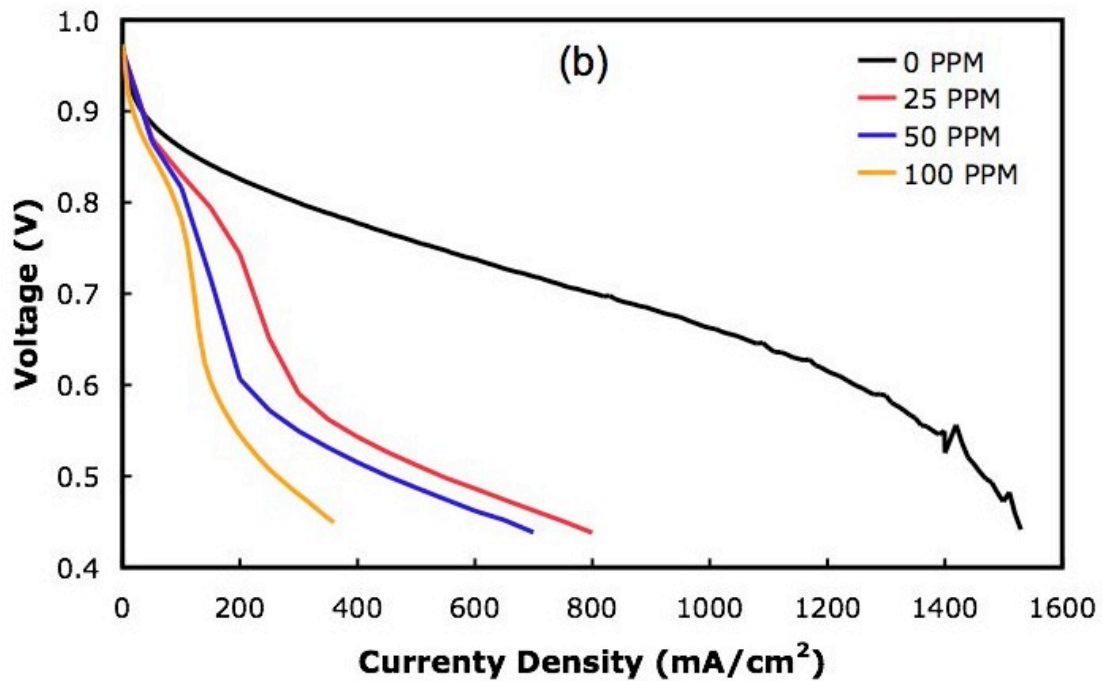
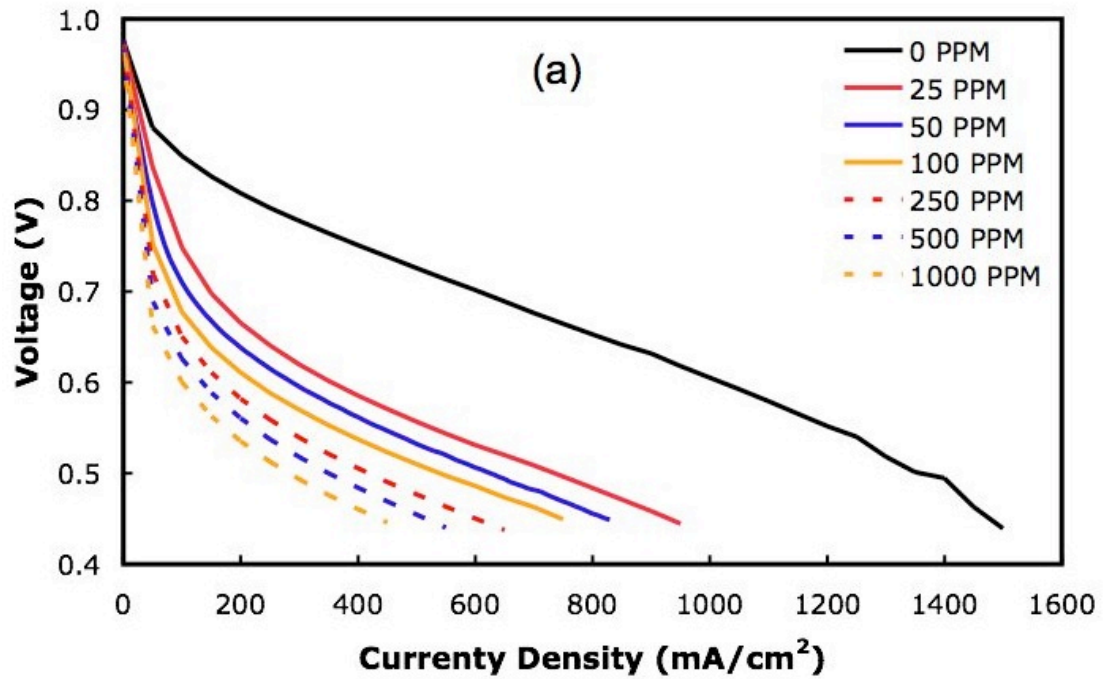


**Figure 3.14:** Polarization data by MEA (a) 7b and (b) 8a potential cycled PtSn anode catalyst with up to 1000 PPM CO. 2.2/2.2 stoichiometry with 0.56/0.133 SLPM minimum flow rates, 70 °C cell temperature with 70 °C anode and cathode dew points

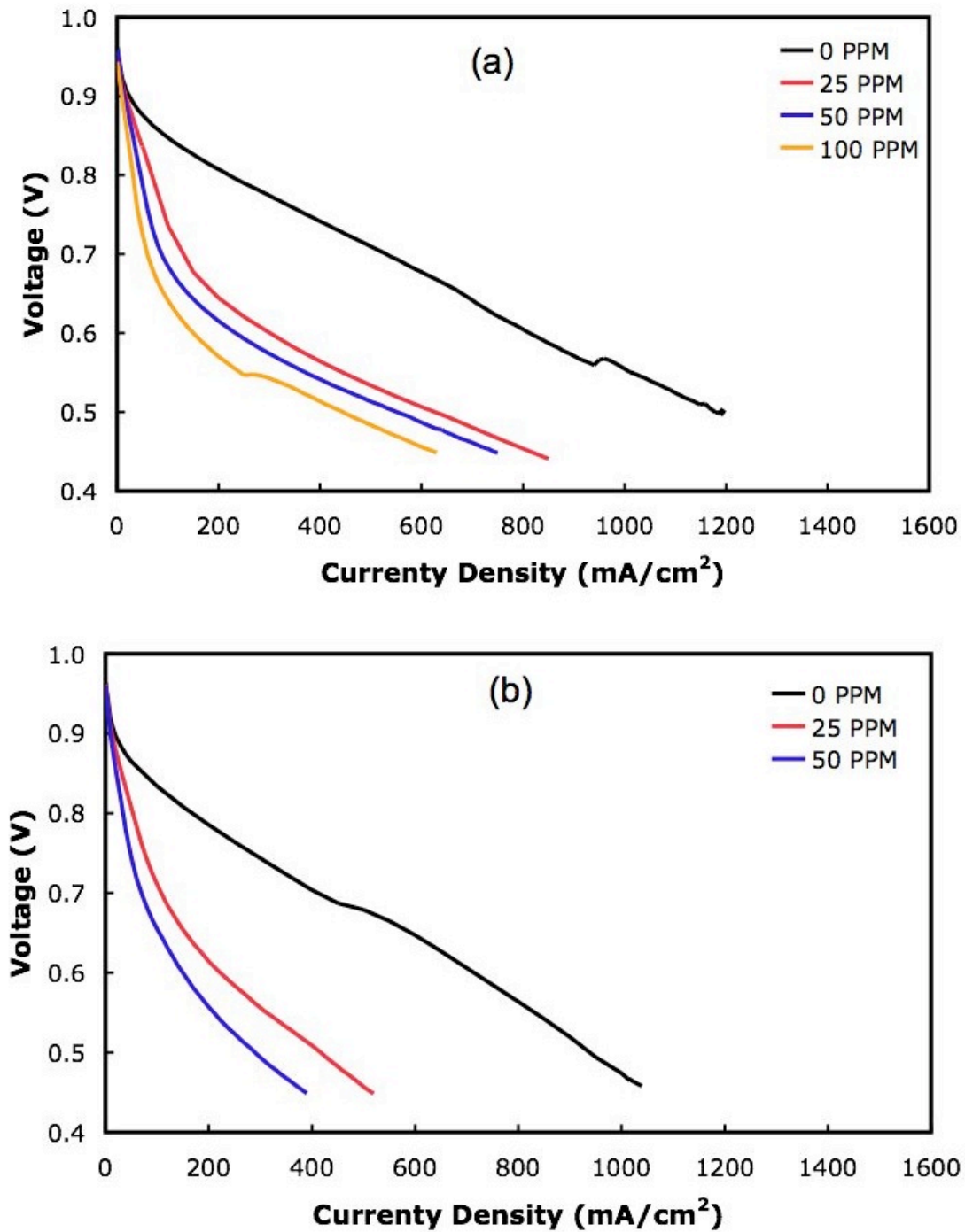


**Figure 3.15:** Polarization data of MEA (a) 8b and (b) 9c, potential cycled PtSn anode catalyst with up to 100 PPM CO. 2.2/2.2 stoichiometry with 0.56/0.133 SLPM minimum flow rates, 70 °C cell temperature with 70 °C anode and cathode dew points

Comparison of cycled MEAs with data from the literature on PtSn intermetallic anode catalysts shows quite similar results both quantitatively and qualitatively. The work of both Lee & Mukerjee (1999) and Lee, Hwang, and Lee (2005) show the same general form of the polarization curve, an initially large drop in voltage when CO is present in the anode fuel followed by a return to the slope of the polarization data from non-CO containing anode fuel. **Figure 3.16** from Lee is an example using PtSn(3:1)/C intermetallic catalyst on the anode that closely resembles the potential cycled MEAs in this study.

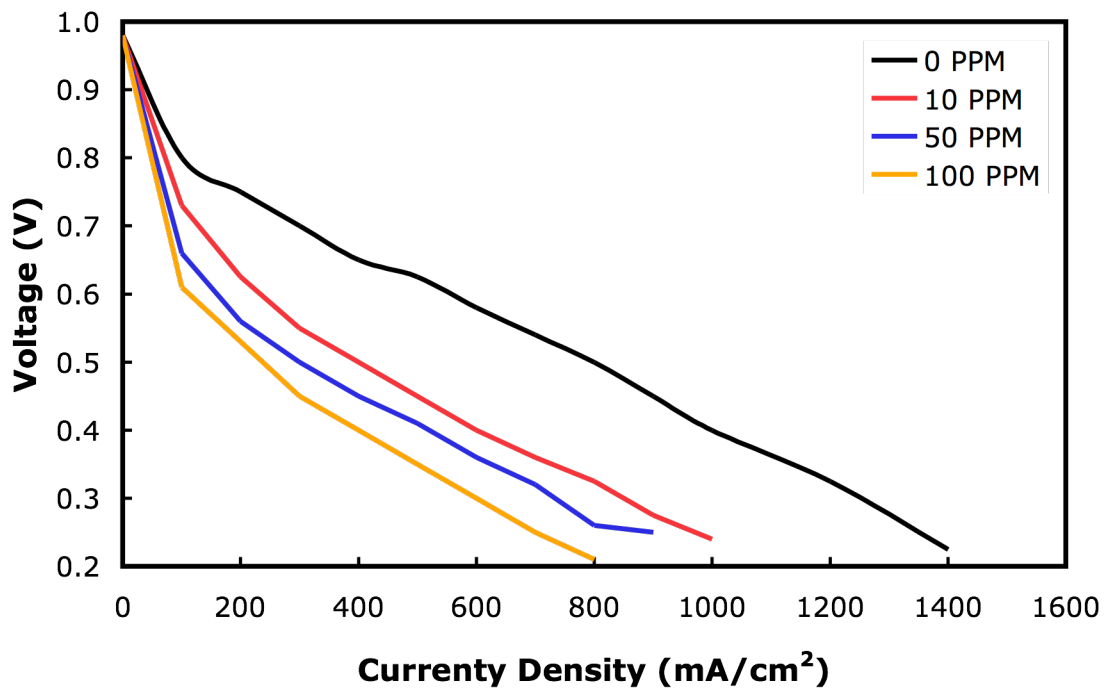


**Figure 3.16:** PtSn(3:1) anode electrocatalyst polarization curve from Lee, Hwang, Lee (2005) at 0 ppm, 10 ppm, 50 ppm, and 100 ppm CO at 80 °C

### 3.2.2 EIS

Electrical impedance spectroscopy can provide insight into the multiple processes occurring simultaneously in a PEM fuel cell MEA. The value of the high frequency intercept of the real axis of the Nyquist plot represents the bulk resistance of the membrane. **Table 3.2** shows the bulk resistance of each MEA at the end of testing. The MEA PtRu anode catalyst exhibited the lowest membrane resistance. The PtSn MEAs showed membrane resistances 8% to 50% higher than MEA 6a. The bulk resistance values either remained constant or decreased with time, suggesting that the potential cycling process is not harmful to the membrane.

**Table 3.1:** Bulk resistance ( $R_{bulk}$ ) of MEAs, calculated from EIS ( $\Omega$ )

MEA	Bulk resistance
PtRu	0.012
7a	0.015
7b	0.013
8a	0.014
8b	0.018
9c	0.014

**Figure 3.17** shows EIS Nyquist plots for galvanostatic measurements from MEAs 7a, 7b, and 9c at 100 and 500 mA/cm<sup>2</sup>. All three demonstrate extremely similar results at 0, 25, 50, and 100 ppm CO. The high frequency intercept of the real axis, occurring at higher impedance than the bulk resistance, is a measure of the polarization resistance of the catalyst layer. This is most certainly true for 100 mA/cm<sup>2</sup>. At 500 mA/cm<sup>2</sup>, the loop begins to divide into two semicircles. The second, smaller semicircle occurring at low frequencies represents a mass transport resistance that begins to arise as higher currents

consume a larger amount of fuel. That fact that the second semicircle is much larger than the first suggests that the resistance represented by the low frequency intercept is still charge transfer dominated. For all three MEAs,  $R_{pol}$  jumps dramatically between 0 and 25 ppm and remains relatively constant through 100 ppm. The low frequency loop crosses the real axis into positive imaginary impedance, exhibiting an inductive-like behavior. This signifies that there are competing adsorption processes present, most likely intermediate species important in the CO oxidation reaction [54, 55, 56, 57]. The trend at 500 mA/cm<sup>2</sup> is identical to 100 mA/cm<sup>2</sup> although the  $R_{pol}$  values are lower in magnitude.

In **Figure 3.18**, MEA 8b demonstrates a similar trend to 7a, 7b, and 9c. MEA 8a at 100 mA/cm<sup>2</sup> shows a decreased charge transfer resistance compared to the other PtSn MEAs at 25 ppm with no inductive behavior. 8a also shows increased  $R_{pol}$  at 100 ppm with inductive behavior. At 500 mA/cm<sup>2</sup> the trend in 8a is the same as all other PtSn MEAs. The PtRu MEA shows much lower  $R_{pol}$  than the PtSn MEAs at both current densities and only shows a dramatic increase in  $R_{pol}$  between 50 and 100 ppm at 500 mA/cm<sup>2</sup>. The mass transfer resistance based low frequency loop is more pronounced at both current densities. The low frequency loop never completely crosses the real axis, meaning that the mechanism of CO tolerance expressed in PtRu at this current is likely not CO oxidation but a preferential H<sub>2</sub> adsorption on the surface of the particle.

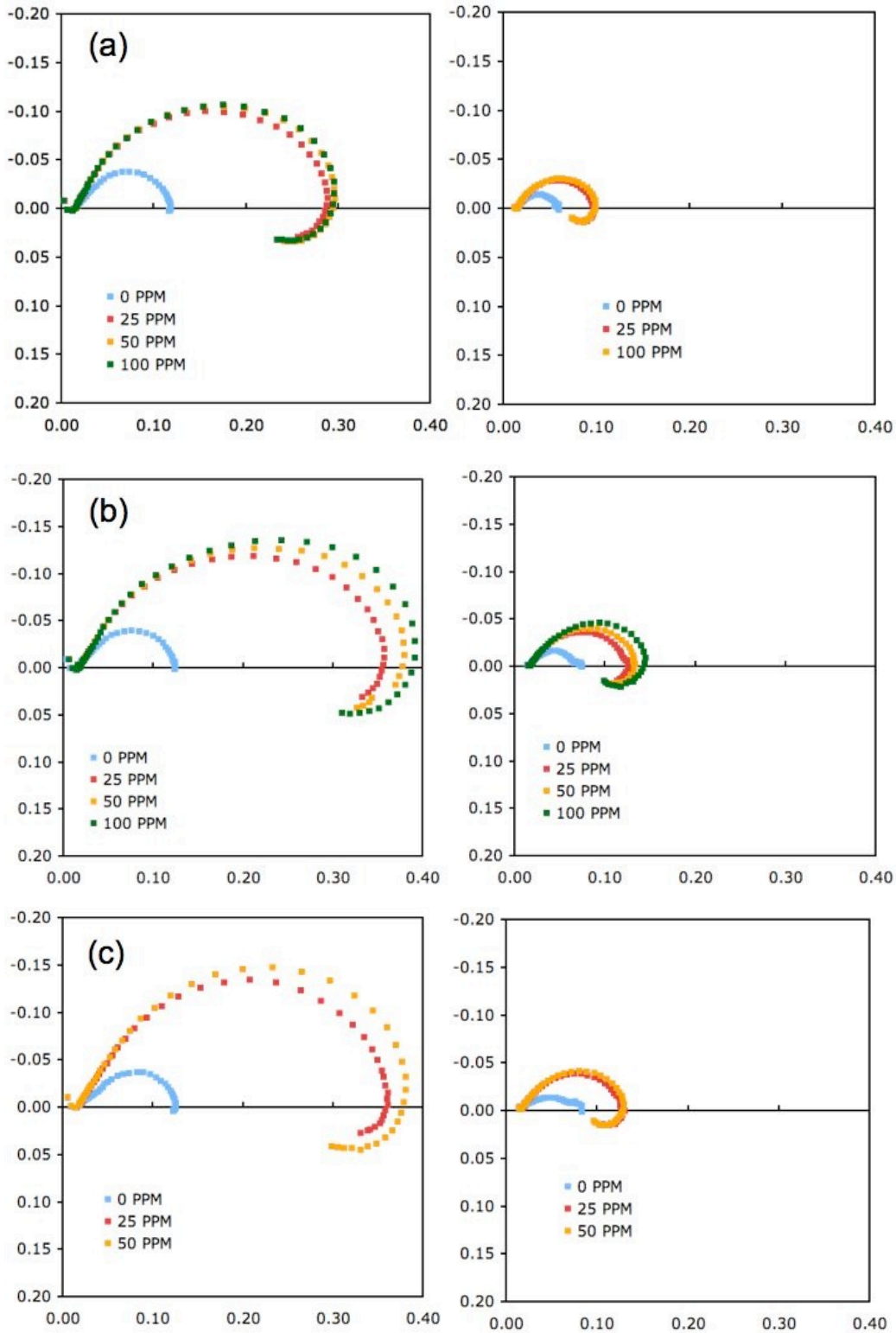


**Figure 3.17:** EIS Nyquist plot of MEAs 7a, 7b, and 9c at a) 100 mA/cm<sup>2</sup> and b) 500 mA/cm<sup>2</sup> under polarization data operating conditions

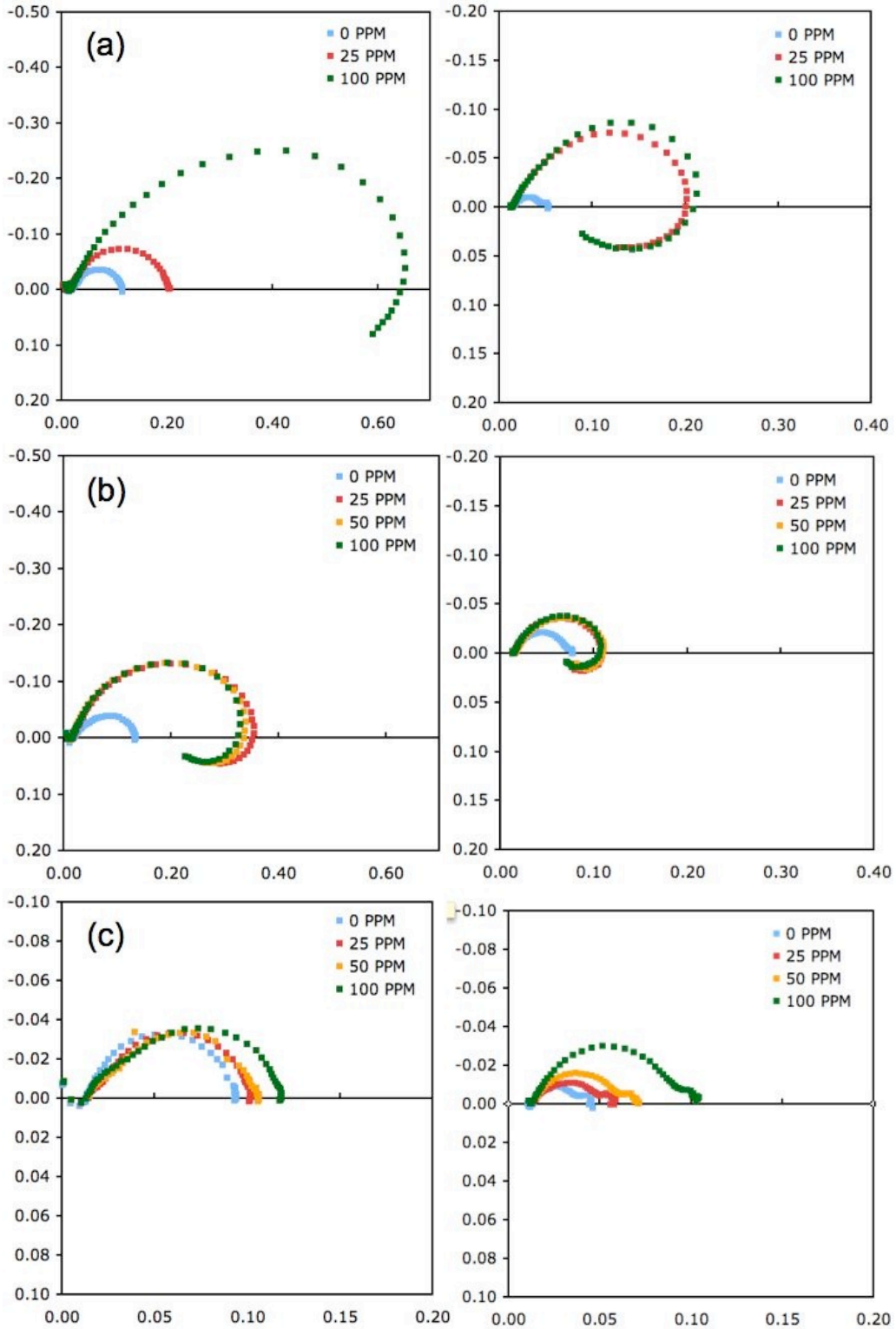


**Figure 3.18:** EIS Nyquist plot of MEAs (a) 8a, (b) 8b, and (c) PtRu at 100 and 500

$\text{mA}/\text{cm}^2$  under polarization data operating conditions

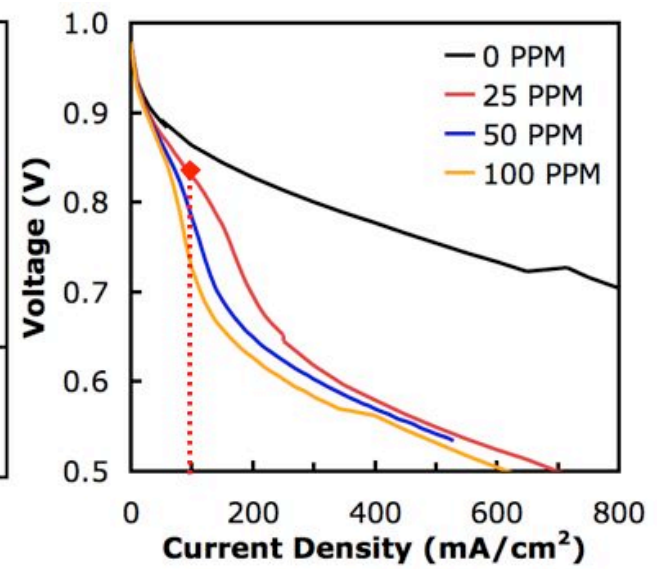
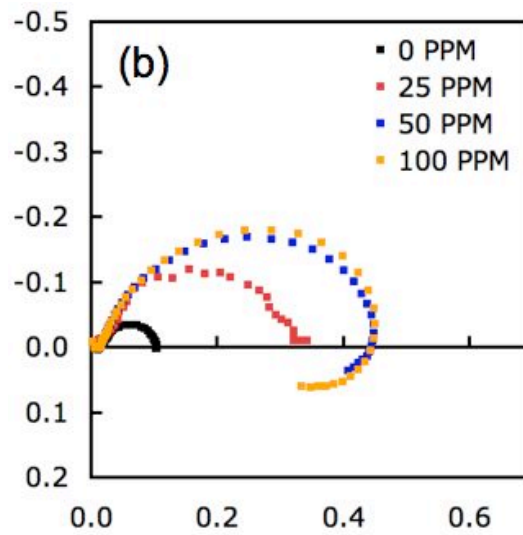
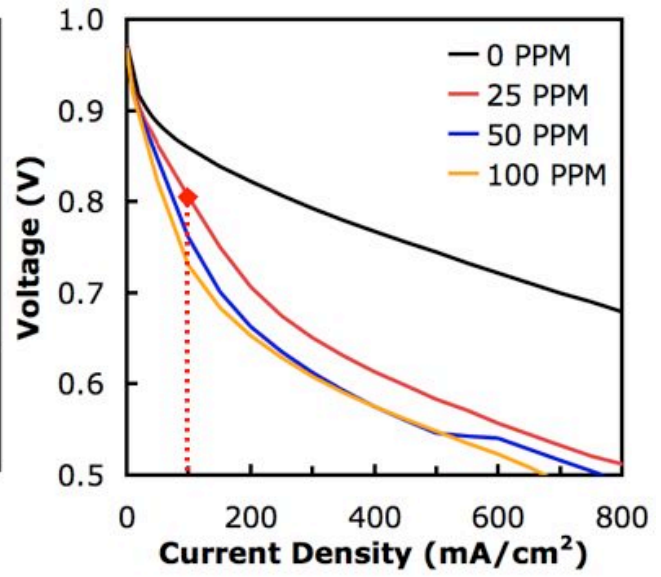
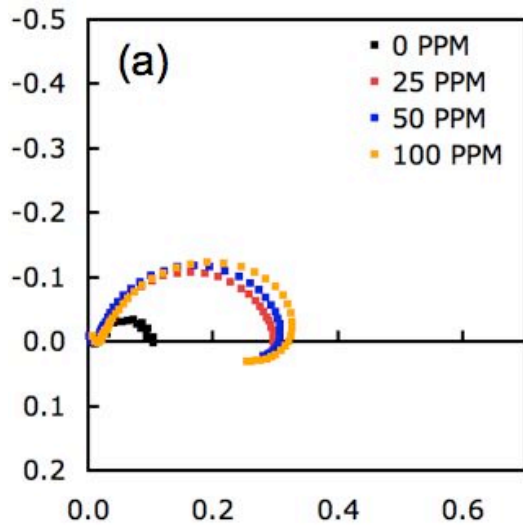
The  $R_{pol}$  values of each MEA using 0 and 25 ppm CO anode fuel are presented in **Table 3.2**.  $R_{pol}$  at both 100 and 500 mA/cm<sup>2</sup> for the PtRu MEA is lower than the PtSn MEAs at all conditions. MEA 7a and 8a show the best  $R_{pol}$  values with pure H<sub>2</sub>. MEA 8a also shows a  $R_{pol}$  smaller than the rest at 100 mA/cm<sup>2</sup> and larger than the rest at 500 mA/cm<sup>2</sup>. The polarization resistance from CO ( $R_{pol,CO}$ ) can be calculated by subtracting the  $R_{pol}$  at 0 ppm from the  $R_{pol}$  at 25 ppm. While PtRu exhibits very small  $R_{pol,CO}$  (0.007 and 0.011  $\Omega$  at each current density), MEAs 7a/7b and 8a/8b exhibit much larger  $R_{pol,CO}$ , on average 0.235  $\Omega$  at 100 mA/cm<sup>2</sup> and 0.067  $\Omega$  at 500 mA/cm<sup>2</sup>.

**Table 3.2:** Polarization resistances at 100 and 500 mA/cm<sup>2</sup>, calculated from EIS ( $\Omega$ )

MEA	0 PPM		25 PPM	
	100 mA/cm <sup>2</sup>	500 mA/cm <sup>2</sup>	100 mA/cm <sup>2</sup>	500 mA/cm <sup>2</sup>
PtRu	0.082	0.033	0.089	0.044
7a	0.103	0.045	0.271	0.083
7b	0.111	0.062	0.341	0.112
8a	0.102	0.038	0.189	0.185
8b	0.115	0.059	0.334	0.091
9c	0.111	0.070	0.346	0.116

Examining the EIS Nyquist plots of MEA 8a at 100 mA/cm<sup>2</sup> as the total number of cycles increased can help explain the slight divergence from the electrochemical behavior of cycled PtSn anode electrocatalysts seen in other MEAs. **Figure 3.19** shows the polarization and EIS Nyquist data of MEA 8a after the 4<sup>th</sup>, 5<sup>th</sup>, and 6<sup>th</sup> cycling sets. The Nyquist plot from 4<sup>th</sup> cycling set shows the same pattern as other cycled PtSn MEAs, a large increase in charge transfer resistance upon the presence of CO that is relatively independent of CO concentration up to 100 ppm. After the 5<sup>th</sup> cycle set, the charge

transfer resistance at 50 and 100 ppm increases while the 25 ppm data set no longer shows inductive like behavior at low frequencies. After the 6<sup>th</sup> cycle set, the charge transfer resistance at 100 ppm increases again, the 50 ppm data set loses inductive like behavior, and the charge transfer resistance at 25 ppm decreases. Matching the Nyquist plots to their respective polarization curves, a sharp drop of about 0.2 V appears to be shifting to the right as the number of cycles increases. The 100 mA/cm<sup>2</sup> data point appears to be in the middle of the voltage drop after the 4<sup>th</sup> set, at the very beginning of the voltage drop after the 5<sup>th</sup> set, and before the voltage drop after the 6<sup>th</sup> set. The sharp drop in voltage can be attributed to overpotentials associated with CO oxidation because the inductive like behavior of the Nyquist plot pertaining to intermediate species in the CO oxidation process disappears when moving from high to low current on the polarization curve. Successive cycles after the 6<sup>th</sup> set did not show any further current shift in the voltage drop.



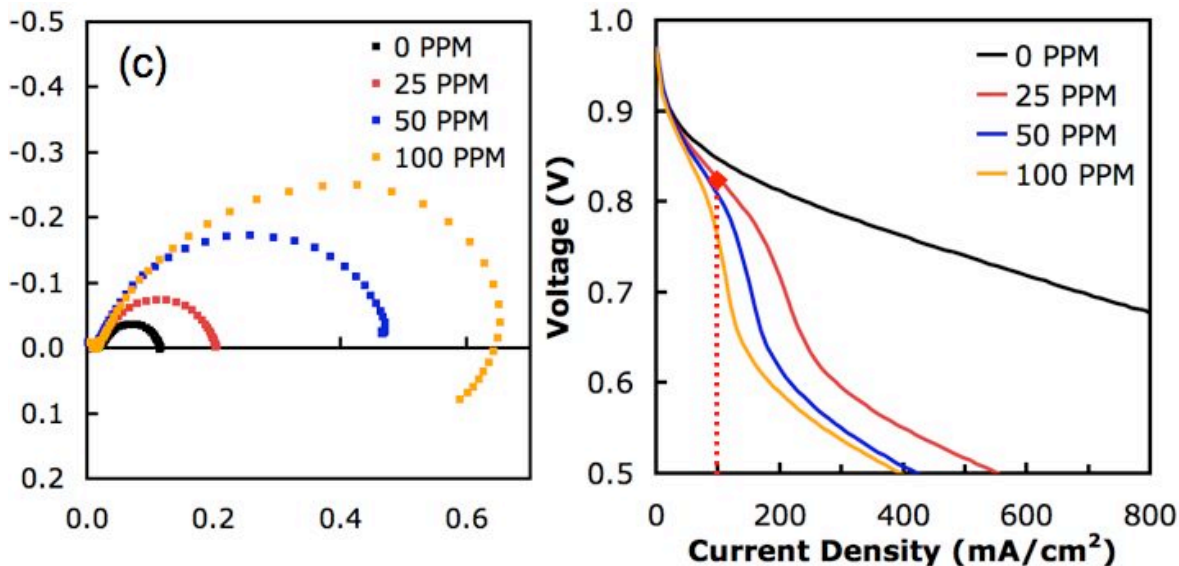


**Figure 3.19:** MEA 8a performance transformation after 4<sup>th</sup>, 5<sup>th</sup>, and 6<sup>th</sup> cycling sets at 0, 25, 50 and 100 ppm: a) Polarization and b) EIS Nyquist plots at 100 mA/cm<sup>2</sup> under polarization data operating conditions

The specific cause of the shift in onset of a significant  $\eta_{CO}$  could be that some adsorption sites are becoming CO tolerant but others are not, leading to a delayed onset of  $\eta_{CO}$  as a function of current density. The change could be occurring on the scale of individual sites on nanocatalyst particles or of the catalyst layer itself. **Figure 3.20** shows how a partially CO tolerant catalyst layer may produce the CO polarization results in MEA 8a. During the cycling process, the catalyst particles closest to the anode flow inlet become CO tolerant whereas those downstream do not due to either a change in gas composition with channel distance or the current density only allowing a portion of the catalyst to be utilized. Normally, current decays exponentially to a minimum value as a function of channel distance. A sudden transition from utilizing CO tolerant catalyst sites to sites greatly affected by CO would cause a sudden drop in current. A partially CO

tolerant anode catalyst layer would not be affected by the presence of CO until the less CO tolerant sites are utilized, creating a delay in the onset of  $\eta_{CO}$ .

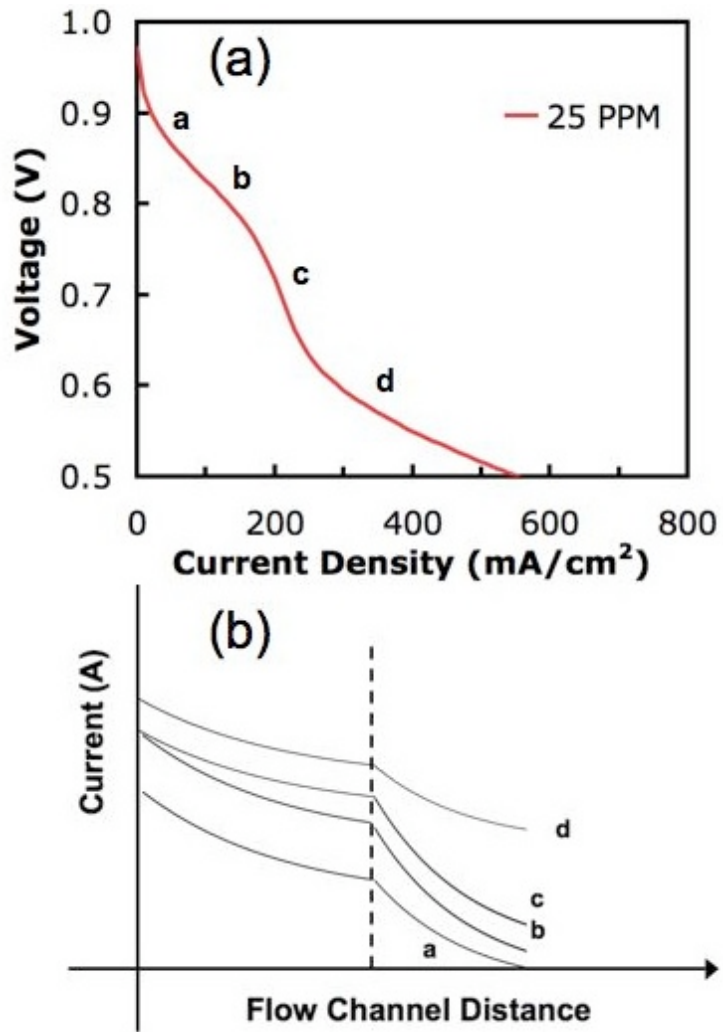


**Figure 3.20:** Shift in onset of  $\eta_{CO}$  – (a) Polarization curve of MEA 8a with 25 PPM CO and (b) Current as a function of anode flow channel distance

### 3.3 Conclusion

The potential cycling of PtSn anode electrocatalysts in the MEA led to different behavior depending on the number of cycle per set, potential cycling range, and anode gas composition. Cycle set length does not greatly change the CO cycling process. The extreme similarity in polarization and EIS data between MEA 7a and 7b, which had identical gas compositions and potential cycling ranges, confirms this. Detailed cycling data from MEA 8b showed that most of the transformation occurs in the first 50 to 100 cycles and the voltage-current relationship barely changes after 200 cycles.

$V_{\text{cell}}$  cycling from OCV to 0 V improved performance with H<sub>2</sub> over cycling to lower voltages (-0.2 V) with identical gas compositions. MEA 8a (with potential cycling to 0 V) showed a larger reduction in the apparent overpotential for CO oxidation and in  $R_{\text{pol}}$  as the number of cycles increased than MEA 8b (with potential cycling to -0.2 V). This shift resulted in lower CO overpotentials at currents less than 300 mA/cm<sup>2</sup> but higher CO overpotentials at higher current densities after the completion of cycling.

Varying the gas composition factor showed little variation in both pure H<sub>2</sub> performance and  $\eta_{\text{CO}}$ . Low CO to water ratios did not produce good CO tolerance or pure H<sub>2</sub> polarization, suggesting that excess water is detrimental to the cycling process, perhaps by interfering with CO adsorption on the surface of the catalyst. Using low CO content, low flow stoichiometry, and H<sub>2</sub> cathode gas during cycling showed improved performance, but a lower pure H<sub>2</sub> polarization curve than standard catalysts and high CO overpotentials. This can be attributed to either the small fraction of CO present for cycling or the H<sub>2</sub> cathode cycling process being less effective than the standard cycling procedure. Having too little or excessively large amounts of CO during cycling is not

effective in producing an active anode electrocatalyst for both H<sub>2</sub> adsorption and CO tolerance. CO and H<sub>2</sub>O flow rates producing a stoichiometric ratio of 1.62 for H<sub>2</sub>O at 1 A produced the best CO tolerance and pure H<sub>2</sub> results. The shift in the voltage drop associated with CO oxidation in MEA 8a suggests that the catalyst layer is being partially converted.

## 4 Ex situ Catalyst Characterization

### 4.1 SEM/EDX of Catalyst Layer

After testing, some of the MEAs were cut into cross-sections and observed using SEM to observe the uniformity and composition of the catalyst layer, as shown in Chapter 2. The freezing and breaking of the MEA during sample preparation process was not always successful in creating a clean cross section with undisturbed catalyst layers that remained attached to the membrane. The cross section of MEA 8a in **Figure 4.1** shows separation between the cathode catalyst layer and GDL as well as GDL and catalyst segments in the membrane region, which likely occurred during the making of the cross-section. The cross section of MEA 8a was still clean enough in other areas to take accurate EDX line scans.



**Figure 4.1:** SEM image of MEA 8a at 300X magnification, catalyst layer separation and dispersed GDL/catalyst segments

There is no membrane discernable in the cross section of MEA 7b in **Figure 4.2**, making distinguishing between the anode and cathode catalyst layers impossible. Although not always successful, the freeze and break procedure to create MEA cross sections was more effective than simply cutting the cross section manually without any freezing.



**Figure 4.2:** SEM image of MEA 7b at 300X magnification, no membrane visible

SEM images generally showed intact membranes with uniform and attached catalysts in large enough sections of the MEA that EDX analysis could be performed. One example of an MEA after fabrication is shown in **Figure 4.3**.

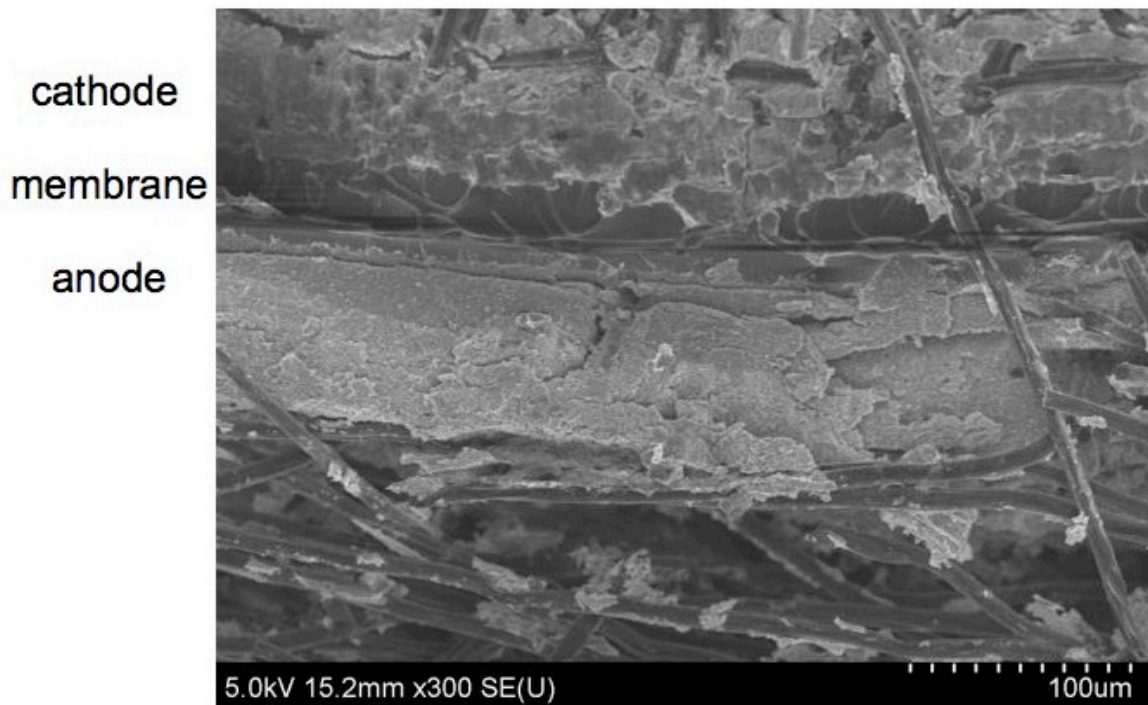


**Figure 4.3:** SEM image of an MEA after fabrication showing intact catalyst layers attached to the membrane at 300X magnification

Only one cross section was taken per MEA and only segments of the cross section could be observed in detail. EDX analyses were performed by scanning along a line perpendicular to the membrane from one GDL to the other that encompassed both catalyst layers. The vertical axis in each plot of the results is the strength of signal as a percent of the strongest signal. The anode and cathode catalyst layers contain equal metal loadings. The largest peak observed is credited to Pt since the cathode contains Pt only and would thus have a higher Pt content than the anode. Multiple line scans on each MEA were performed in different locations to ensure that the features observed were not local effects. The membrane generates no signal during the EDX line scan because the membrane is not electrically conductive, a property necessary for EDX analysis to generate the emissions necessary for a detectable signal. **Figure 4.4** displays

the EDX line scan of a PtSn intermetallic anode electrocatalyst MEA after fabrication but without potential cycling. The cathode segment contains a large Pt signal and an Sn signal that does not rise above the noise level seen in the membrane. The anode shows a smaller Pt content than the cathode as well as the presence of Sn. The relative signal strengths are not reflective of the ratio of Pt to Sn, which is known to be 1:1 from TEM analysis of the catalyst as manufactured. The Sn signal is low in the anode, but sufficiently above the noise level to confirm that Sn is present there and that it is not present in the cathode. EDX line scans of the untested MEA were used as the standard to which EDX line scans of tested MEAs were compared.

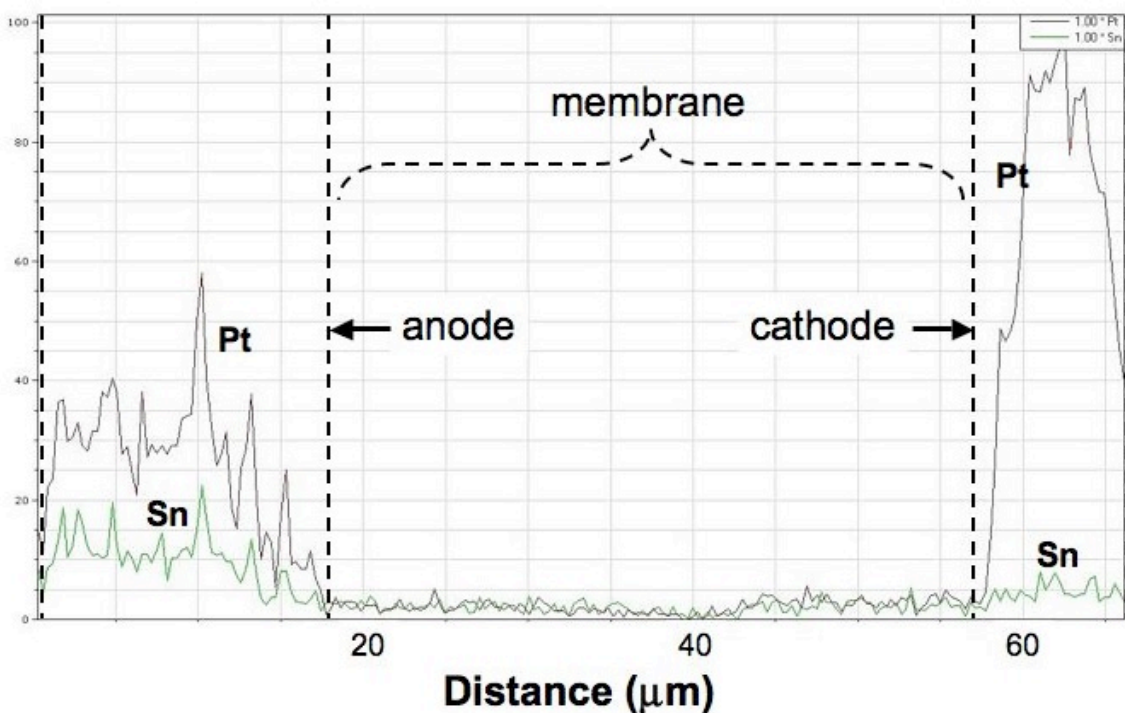


**Figure 4.4:** EDX analysis of PtSn MEA before testing, Pt and Sn content by location

**Figure 4.5** displays the EDX line scan of MEA 4b after testing. The Pt signals in both the anode and cathode appear in the same ratios here as they do for the baseline test.

The Sn signal in the anode is the same as the baseline. Sn also appears in the cathode, appearing in an amount on par with the peak Sn signal in the anode and located at the interface between the membrane and the catalyst layer. The Sn signal decreases at locations further away from the membrane. Since the only possible source of Sn is the anode catalyst layer, the CO cycling process must have encouraged the leaching of Sn atoms across the membrane to the cathode side. The decrease in concentration of Sn at locations further from the membrane-cathode interface suggests this as well.

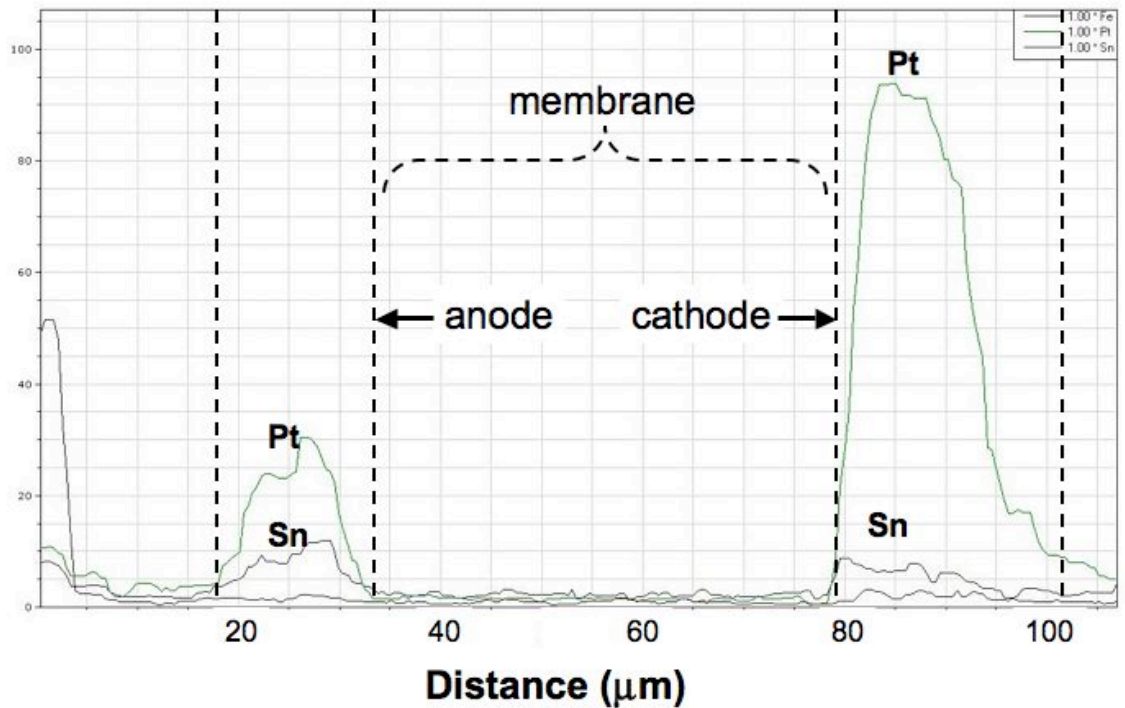


**Figure 4.5:** EDX analysis of MEA 4b after testing, Pt and Sn content by location

**Figure 4.6** shows the EDX line scan of MEA 8a. The Pt signals in both the anode and cathode are equivalent, suggesting that some Pt degradation may have occurred in the cathode catalyst layer. The Sn signal in both the anode and cathode are virtually

equivalent, suggesting that a large amount of Sn has migrated to the cathode during the CO cycling process. MEA 8a was subjected to a total of 2200 cycles whereas MEA 4b was subjected to only 1000 total cycles.

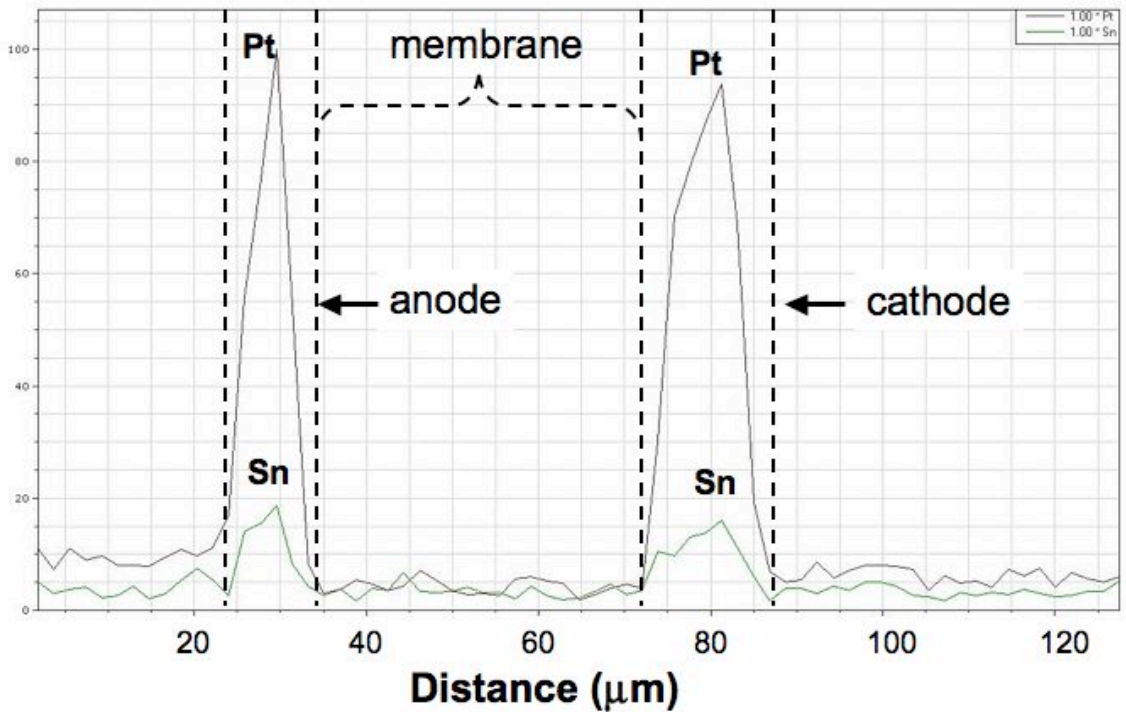


**Figure 4.6:** EDX analysis of MEA 8a after testing, Pt and Sn content by location

**Figure 4.7** shows the EDX line scan for MEA 9c. The Pt signals in both the anode and cathode resemble the baseline case. However, there is no Sn signal in the anode and a Sn signal only slightly above the noise level in the cathode. This trend was observed in multiple line scans in different locations on MEA 9c, suggesting that the absence of Sn is not a local feature. 9c was subjected to a total of 3200 cycles with a high CO concentration, an amount of cycles much larger than any other MEA. The final destination of Sn in the MEA is unknown, perhaps dispersed in the GDL. It is not likely

that significant amounts of Sn particles reside in the membrane because bulk resistance determined from EIS experiments did not degrade with time.

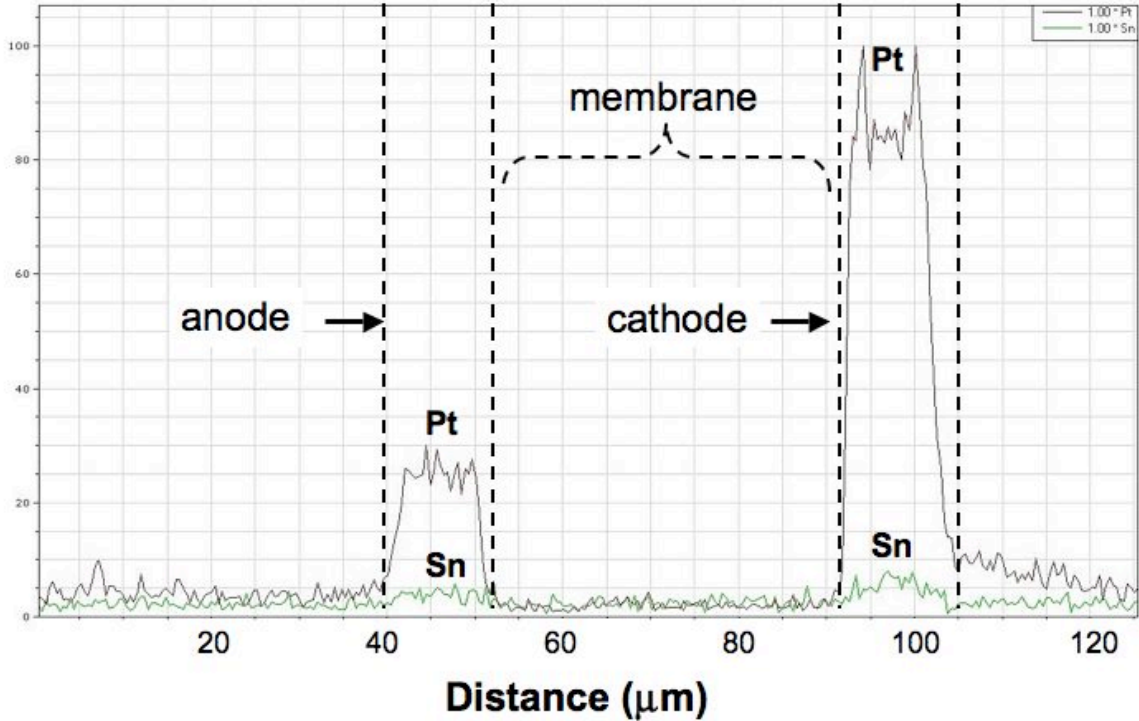


**Figure 4.7:** EDX analysis of MEA 9c after testing, Pt and Sn content by location

Observed membrane thicknesses in this section 5 to 20 μm less than 50 μm, the thickness of Nafion membrane material as received. Membranes observed to be within 5 μm of the specified thickness could be explained by a statistical variation. Membranes observed to be greater than 10 μm less than the specified thickness could have been slightly compressed during the hot pressing process or compression of the MEA in the test fixture.

## 4.2 Conclusion

Ex situ characterization of MEAs after cycling show that the composition of both the anode and cathode catalyst layers change as the number of cycles increase. The anode leaches Sn particles, which travel across the membrane to the cathode catalyst layer. As the number of cycles increases, more Sn particles migrate to the cathode until the anode is depleted of Sn particles and the cathode begins to lose Sn particles as well. The effect appears to affect all MEAs regardless of gas composition, voltage range, and cycle set length.

These results imply that the CO cycling process is more of a surface dealloying process than a structural reforming process. Sn particles are being removed from the surface of the nanoparticles and are encouraged to transport across the membrane to the cathode either by the electric field created during the CO cycling process or by the water necessary for proton transport across the membrane. The CO cycling process may still be enacting structural changes while removing Sn atoms, as is suggested by the change in CO tolerance behavior of MEA 8a. If so, these changes are not significant enough to create nanoparticle structures for higher CO tolerance. The final structure of individual nanoparticles cannot be determined directly through EDX analysis performed by TEM because the bond between the catalyst layer and membrane created during hot pressing precludes obtaining a usable sample. The electrochemical data suggests that the structure remains intermetallic from comparison with electrochemical results from past studies.

## 5 Conclusions

This study explored the effect of MEA potential cycling on enhancing CO tolerance of PtSn intermetallic anode electrocatalysts. The study was motivated by RDE experiments that showed significant reduction of CO oxidation potentials on PtSn intermetallic electrocatalysts that occurred after hundreds of potential cycles in the presence of 1000 ppm CO in H<sub>2</sub>. This CO oxidation enhancement was determined to be caused by the formation of a core-shell PtSn@Pt electrocatalyst, and the PtSn core is presumed to shift the d-band center of the Pt to promote electrochemical CO oxidation at low-temperature [33]. An equivalent procedure was designed for PEM fuel cell MEAs and executed with varying operating conditions to observe their effect on the PtSn anode electrocatalyst. The potential cycled MEAs were tested for electrochemical performance both during and at the end of the cycling process with anode flows containing up to 1000 ppm CO. Electrochemical data collected at the end of cycling was compared to that of an MEA fabricated with PtRu(1:1.5) anode electrocatalyst. The MEAs were examined after testing using SEM/EDX to analyze the properties of the catalyst layer and look for Sn migration.

### 5.1 Significant Results and Impact on PEM Fuel Cell Systems

PtSn intermetallic catalysts were successfully fabricated and applied to PEM fuel cell MEAs. A potential cycling procedure was designed for PEM fuel cells to simulate conditions of RDE potential cycling experiments using liquid electrolyte in the presence of 1000 ppm CO. It was hoped that the potential cycling procedure would create the active PtSn@Pt structure from PtSn intermetallic. Potential cycling of PtSn intermetallic

anode catalysts show that CO is adsorbed on the catalyst surface, oxidized as the anode potential increases, and readsorbed as the potential decreases back to OCV. The voltage-current relationship over the cycle approaches a steady state after 50 to 100 cycles. Changing the number of cycles between electrochemical characterizations does not significantly affect polarization or EIS results after cycling has been completed at ranges above 200 cycles. Cycling the potential to a minimum cell voltage of -0.2 V generated an estimated anode potential of 0.7 V relative to its OCV value with CO, a range matching RDE cycling experiments. Polarization and EIS after cycling showed that cycling using this range showed decreased H<sub>2</sub> performance and higher CO overpotentials at low currents but lower CO overpotentials at high currents when compared to a smaller cycling potential range.

Anode gas composition containing equal amounts of CO and H<sub>2</sub>O for the CO oxidation reaction at stoichiometric ratios of 1.5 at 1 A produces the highest currents of all MEAs with pure H<sub>2</sub> (1250 mA/cm<sup>2</sup> at 0.6 V) and lower CO overpotentials at currents less than 200 mA/cm<sup>2</sup> when used with the smaller voltage range. Very low CO overpotentials at higher current densities were seen in MEA 7a and 7b but with increased pure H<sub>2</sub> overpotentials. MEAs cycled using a stoichiometric ratio for H<sub>2</sub>O of 1.62 at 1 A showed the lowest CO overpotentials. MEAs cycled with higher or lower stoichiometric ratios for H<sub>2</sub>O at 200 mA/cm<sup>2</sup> showed higher overpotentials both with and without CO, which suggests that H<sub>2</sub>O content is critical to the potential cycling process. The choice of either H<sub>2</sub> or N<sub>2</sub> as the balance gas does change the potential cycle because CO adsorption and oxidation predominate over H<sub>2</sub> adsorption at anode CO concentrations of 1% or greater. CO overpotentials at all currents for cycled PtSn intermetallics are reflective of

PtSn intermetallics without potential cycling from previous studies. These CO overpotentials were larger than PtRu(1:1.5) but smaller than Pt.

SEM images using EDX analysis showed that Sn content increased in the cathode as the number of potential cycles increased. Under the conditions in this study, the potential cycling procedure promotes Sn leaching out of the anode catalyst layer, across the membrane, and into the cathode catalyst layer. Despite the presence of Sn in the cathode, MEA 8a exhibits a current of 1250 mA/cm<sup>2</sup> at 0.6 V after 2200 cycles, suggesting that the presence of Sn does not hamper the ability of the cathode catalyst layer to execute the ORR.

Although RDE potential experiments suggested that potential cycled PtSn intermetallic catalyst could function as a CO tolerance anode electrocatalyst, they did not exhibit CO tolerance when potential cycled under similar conditions in a PEMFC. Differences in conditions between the two experiments such as electrolyte composition or the presence of the ORR on the cathode in PEMFCs may prevent the CO tolerance results from RDE experiments from translating to PEMFCs.

## **5.2 Recommendations for Future Work**

Analysis of the anode catalyst layer after testing was limited to a sample size sufficient for SEM but too large for TEM. TEM would have been the preferred method of detecting catalyst structure since individual particles and the distribution of elements therein are possible through TEM whereas SEM can only determine elemental distributions over the catalyst layer. Hot pressing of the MEA creates a permanent attachment between the GDEs and the membrane, providing a smooth catalyst layer/ionomer interface but preventing the removal of catalyst particles for TEM samples.

X-ray photoelectron spectroscopy (XPS) could be used to determine the oxidation state of Sn in the anode, which may provide some insight into the catalyst nanoparticle structure and the role that Sn plays in CO adsorption and oxidation.

Methods of creating PtSn@Pt core-shell nanoparticles without potential cycling should be examined. The potential cycling procedure was designed to eliminate the possibility of surfactants interfering with the catalyst-membrane interface of the anode in a PEMFC. Alternative catalyst fabrication methods could result in stable PtSn@Pt catalysts without surfactants. If surfactants are necessary to create the PtSn@Pt core-shell structure, new treatment methods could remove the surfactants without modifying the core-shell structure.

Although this study did not result in the production of a highly CO tolerant PtSn anode electrocatalyst through potential cycling, similar processes in PEMFCs with other catalysts could do so. The process itself can be improved by designing a single cell PEM MEA test fixture that allows for cycling with a reference electrode design [58]. Using a fixed standard eliminates the contribution of cathode overpotentials to the potential cycling range. CO tolerance conclusions about anode electrocatalysts from RDE experiments do not always translate into PEMFCs. The differences between anode electrocatalyst CO tolerance in RDE and PEMFC experiments must be identified in order for RDE testing to be a useful indicator of CO tolerance in anode electrocatalysts. Doing so will help in the future research of possible anode electrocatalysts for use in PEMFCs.

If CO tolerant anode electrocatalysts are discovered through single cell MEA testing at various operating conditions, they should be tested in large PEMFC stacks to determine their effectiveness in a full PEMFC system. CO tolerant anode electrocatalysts

should decrease the cost of hydrocarbon fueled PEMFC systems, making them competitive in the transportation and portable power markets.

## Bibliography

1. Srinivasan, Supramaniam. Fuel Cells: From Fundamentals to Applications. Springer, (2006).
2. Larminie, James, and Andrew Dicks. Fuel Cell Systems Explained. J. Wiley, (2003).
3. Mengel, C et al. *Journal of Fuel Cell Science and Technology* 5:2, 1-5 (2008).
4. Ersoz, Olgun, Ozdogan Ersoz, Atilla, Hayati Olgun, and Sibel Ozdogan. *Journal of Power Sources* 154.1, 67-73 (2006).
5. Jannelli, Minutillo, Galloni Jannelli, E., M. Minutillo, and E. Galloni. *Journal of Fuel Cell Science and Technology* 4.4, 435-440 (2007).
6. Cheng, Xuan et al. *Journal of Power Sources* 165.2, 739-756 (2007).
7. Majlan, Edy Herianto et al. *International Journal of Hydrogen Energy* 34.6, 2771-2777 (2009).
8. M. J. Kahlich, H. A. Gasteiger, and R. J. Behm, *Journal Of Catalysis* 182:430 (1999).
9. F. Marino, C. Descorme, and D. Duprez, *Applied Catalysis B-Environmental* 54:59 (2004).
10. F. Marino, C. Descorme, and D. Duprez, *Applied Catalysis B-Environmental* 58:175 (2005).
11. H. A. Gasteiger, J. E. Panels, and S. G. Yan, *Journal of Power Sources* 127:162 (2004).
12. B. Rohland and V. Plzak, *Journal of Power Sources* 84:183 (1999).
13. Kallitsis, Joannis K, Maria Geormezi, and Stylianos G Neophytides. *Polymer International* 58.11, 1226-1233 (2009).
14. Gourdoupi, N., J.K. Kallitsis, and S. Neophytides. *Journal of Power Sources* 195.1, 170-174 (2010).
15. Kim, Jeong-Hi et al. *Journal of Power Sources* 170.2, 275-280 (2007).
16. Korsgaard, Anders R. et al. *Journal of Power Sources* 162.1, 239-245 (2006).
17. Innocente, A.F., and A.C.D. Ângelo. *Journal of Power Sources* 175.2, 779-783 (2008).

18. Elezovic, Gajic-Krstajic, Radmilovic, Vracar, Krstajic Elezovic, N.R. et al. *Electrochimica Acta* 54.4, 1375-1382 (2009).
19. Divisek, J et al. *Electrochimica Acta* 43.24, 3811-3815 (1998).
20. Baschuk, JJ, and XG Li *International Journal of Energy Research* 25.8, 695-713 (2001).
21. Oetjen, HF et al. *Journal of the Electrochemical Society* 143.12, 3838-3842 (1996).
22. Franco, AA et al. *Electrochimica Acta* 54.22, 5267-5279 (2009).
23. Das, Reis, Berry Das, SK, A Reis, and KJ Berry. *Journal of Power Sources* 193.2, 691-698 (2009).
24. Pereira, LGS, VA Paganin, and EA Ticianelli. *Electrochimica Acta* 54.7, 1992-1998 (2009).
25. Camara, G. A. et al. *Journal of The Electrochemical Society* 149.6, A748-A753 (2002).
26. Lee, S. J. et al. *Electrochimica Acta* 44.19, 3283-3293 (1999).
27. Roth, C. et al. *Journal of Electroanalytical Chemistry* 581.1, 79-85 (2005).
28. Jiang, L. et al. *Electrochimica Acta* 53.2, 377-389 (2007).
29. Arenz, Matthias et al. *Journal of the American Chemical Society* 127.18, 6819-6829 (2005).
30. Liu, P., A. Logadottir, and J. K. Nørskov. *Electrochimica Acta* 48.25-26, 3731-3742 (2003).
31. Davies, J.C. et al. *International Journal of Mass Spectrometry* 291.3, 152-158 (2010).
32. Liu, Zhufang, Greg S Jackson, and Bryan W Eichhorn. *Angewandte Chemie* 122.18, 3241-3244 (2010).
33. Nilekar, Anand Udaykumar et al. *Journal of the American Chemical Society* 132.21, 7418-7428 (2010).
34. Wang, Guoxiu et al. *Journal of Alloys and Compounds* 503.1, L1-L4 (2010).
35. Ma, Yuanwei et al. *Catalysis Communications* 11.5, 434-437 (2010).
36. Lebedeva, NP, and GJM Janssen. *Electrochimica Acta* 51.1, 29-40 (2005).

37. Lim, Dong-Ha et al. *Applied Catalysis B: Environmental* 89.3-4, 484-493 (2009).
38. Lee, Dokyol, Siwoo Hwang, and Insung Lee. *Journal of Power Sources* 145.2, 147-153 (2005).
39. Dupont, Celine, Yvette Jugnet, and David Loffreda. *Journal of the American Chemical Society* 128.28, 9129-9136 (2006).
40. Takahashi, I, and SS Kocha. *Journal of Power Sources* 195.19, 6312-6322 (2010).
41. Roche, I et al. *Journal of Physical Chemistry C* 111.3, 1434-1443 (2007).
42. Gasteiger, HA et al. *Applied Catalysis B-Environmental* 56.1-2, 9-35 (2005).
43. Srivastava, R, P Mani, and P Strasser. *Journal of Power Sources* 190.1, 40-47 (2009).
44. Mani, P, R Srivastava, and P Strasser. *Journal of Physical Chemistry C* 112.7, 2770-2778 (2008).
45. Strasser, P, S Koha, and J Greeley. *Physical Chemistry Chemical Physics* 10.25, 3670-3683 (2008).
46. Han, BC et al. *Physical Review B* 72.20 (2005).
47. Hu, Jennifer Ezu. M.S. thesis U of Maryland, College Park, (2009)
48. Hui, C.L., X.G. Li, and I.-M. Hsing. *Electrochimica Acta* 51.4, 711-71 (2005).
49. Zhang, SS et al. *Journal of Power Sources* 194.2, 588-600 (2009).
50. Chen, Gasteiger, Hayakawa Chen, S et al. *Journal of the Electrochemical Society* 157.1, A82-A97 (2010).
51. Promislow, Keith, and Brian Wetton. *SIAM Journal on Applied Mathematics* 70.2, 369 (2009).
52. Cheng, Xuan et al. *Journal of Power Sources* 165.2, 739-756 (2007).
53. Adams, W.A. et al. *Journal of Power Sources* 145.1, 55-61 (2005).
54. Leng, Yong-Jun, Xin Wang, and I-Ming Hsing. *Journal of Electroanalytical Chemistry* 528.1-2, 145-152 (2002).
55. Ciureanu, Mariana, Hong Wang, and Zhigang Qi. *The Journal of Physical Chemistry B* 103.44, 9645-9657 (1999).

56. Ciureanu, M., S. D. Mikhailenko, and S. Kaliaguine. *Catalysis Today* 82.1-4, 195-206 (2003).
57. Muller, JT, PM Urban, and WF Holderich. *Journal of Power Sources* 84.2, 157-160 (1999).
58. He, W., & Van Nguyen, T. *Journal of The Electrochemical Society*, 151.2, A185-A195 (2004).